

A case study on the origin of near-Earth plasma

A. Glocer¹, D. Welling², C. R. Chappell³, G. Toth⁴, M.-C. Fok¹, C. Komar^{1,7}, S.-B. Kang^{1,7}, N. Buzulukova^{1,8}, C. Ferradas^{1,7}, S. Bingham⁵, and C. Mouikis⁶

¹NASA/GSFC, Greenbelt, MD, USA

²University of Texas at Arlington, Arlington, TX, USA

³Vanderbilt University, Nashville, TN, USA

⁴Climate and Space Sciences and Engineering, University of Michigan, Ann Arbor, MI, USA.

⁵Johns Hopkins University Applied Physics Laboratory (Deceased), Laurel, MD, USA

⁶University of New Hampshire, Durham, NH, USA

⁷Catholic University of America, Washington D.C., USA

⁸University of Maryland, College Park, MD, USA

Key Points:

- Ionospheric H⁺ is a critically important contributor to the magnetosphere during a storm.
- Seasonal effect on outflow create asymmetric filling of the lobes.
- The inclusion of an additional plasmaspheric fluid has system-wide effects.

This is the author manuscript accepted for publication and has undergone full peer review but has not been through the copyediting, typesetting, pagination and proofreading process, which may lead to differences between this version and the [Version of Record](#). Please cite this article as doi: [10.1029/2020JA028205](https://doi.org/10.1029/2020JA028205)

Corresponding author: A. Glocer, alex.glocer-1@nasa.gov

Abstract

This study presents simulations of the coupled space environment during a geomagnetic storm that separates the different sources of near-Earth plasma. These simulations include separate fluids for solar wind and ionospheric protons, ionospheric oxygen, and the plasmasphere. Additionally, they include the effects of both a hot ring current population and a cold plasmaspheric population simultaneously for a geomagnetic storm. The modeled ring current population represents the solution of bounce-averaged kinetic solution; the core plasmaspheric model assumes a fixed temperature of 1eV and constant pressure along the field line. We find that during the storm, ionospheric protons can be a major contributor to the plasmasheet and ring current, and that ionospheric plasma can largely displace solar wind protons in much of the magnetosphere under certain conditions. Indeed, the ionospheric source of plasma cannot be ignored. Significant hemispheric asymmetry is found between the outflow calculated in the summer and winter hemispheres, consistent with past observations. That asymmetric outflow is found to lead to asymmetric filling of the lobes, with the northern (summer) lobe receiving more outflow that has a higher proportion of O^+ and the southern (winter) lobe receiving less outflow with a higher proportion of H^+ . We moreover find that the inclusion of the plasmasphere can have a system-wide impact. Specifically, when the plasmasphere drainage plume reaches the magnetopause, it can reduce the reconnection rate, suppress ionospheric outflow and change its composition, change the composition in the magnetosphere, and reduce the ring current intensity.

1 Introduction

Throughout much of the early space age, it was generally accepted that the solar wind was the source of most of the magnetospheric plasma, with the exception of the plasmasphere which had a composition and temperature matching the underlying ionosphere. That assumption began to change in the early 1970s, first with the discovery of the H^+ polar wind by the Explorer 31 and ISIS 2 satellites [Brinton *et al.*, 1971; Hoffman, 1970; Hoffman *et al.*, 1974], and then with the observation of energetic O^+ raining down out of the magnetosphere [Shelley *et al.*, 1972]. These latter observations were particularly compelling as the ionosphere is the only source of O^+ , and its presence therefore constitutes unambiguous proof of the ionospheric supply of plasma to the magnetosphere. It has since been argued that plasma of ionospheric origin is pervasive throughout geospace, and may at times be the dominant source of plasma in the magnetosphere [Lennartsson *et al.*, 1981; Chappell *et al.*, 1987]. Since these discoveries, the origin of near-Earth plasma and the relative importance of the solar wind and ionosphere to its supply has been an area of fundamental importance and keen scientific interest.

In the study of ionospheric outflow there is often a disproportionate focus on heavy O^+ ions as opposed to the lighter protons. The emphasis on O^+ is understandable as it is clear evidence of ionospheric outflow, but it can give the mistaken impression that protons in the magnetosphere are primarily from the solar wind. While it is true that solar wind protons enter the magnetosphere via reconnection and interaction on the flanks, they are also constantly flowing out of the high latitude ionosphere via the polar wind and filling the lobes [e.g., Axford, 1968]. Indeed, Seki *et al.* [2003] postulated, and recent observations from the Cluster satellites demonstrate, that there is a significant cold population of ionospheric plasma in the magnetosphere [Engwall *et al.*, 2009; Andre and Cully, 2012]. This initially cold population does not necessarily remain cold and may gain significant energy in the magnetosphere and contribute significantly to the magnetospheric proton population. This fact was demonstrated by Huddleston *et al.* [2005] by combining observed polar wind H^+ from the Polar satellite with simulated particle tracing in empirical magnetic fields. They showed that a polar wind proton starting at less than 1 eV was able to gain multiple keV of energy by the time it reached the plasmasheet and ring current.

68 Further complicating this picture is that it is impossible to determine the origin of
69 any particular proton observed in the magnetosphere. However, it is possible to gain some
70 understanding of the origin of magnetospheric protons in the aggregate using observa-
71 tions. One technique involves comparing the ratio of protons to other minor ions in the
72 solar wind, and assuming that similar ratios hold for solar wind protons that make it into
73 the magnetosphere. Using this approach, *Gloeckler and Hamilton* [1987] estimate that as
74 much as 65% of the proton population in the magnetosphere during geomagnetic storms
75 is of ionospheric origin. Additional estimations of the fraction of geogenic plasma in the
76 plasmashet are discussed by *Peterson* [2002]. One of the studies discussed, from *Shelley*
77 *et al.* [1986] and *Shelley* [1986], estimates that under 10% of plasma in the plasmashet
78 originates in the ionosphere during quiet times, but that fraction rises to more than 50%
79 during active times which is consistent with the estimate of *Gloeckler and Hamilton* [1987].
80 A number of assumptions go into this estimate, but of particular relevance to the present
81 discussion is that they separate the ionospheric and solar wind protons by combining the
82 empirical ratio of escaping H^+ and O^+ with the oxygen ion density in the plasmashet.

83 Aside from observations, global models have proven to be a valuable tool in the
84 study of the origin of near-Earth plasma. These models can be loosely broken down into
85 two categories. The first category, involves models that track large numbers of test parti-
86 cles, launched from the ionosphere, through either empirical or single fluid magnetohydro-
87 dynamics (MHD) fields [e.g., *Perroomian et al.*, 2007; *Moore et al.*, 2005]. This approach
88 does not allow particles and fields to evolve self-consistently, but has advantage of includ-
89 ing kinetic effects or non-Maxwellian particle distributions. The second category, involves
90 using a fluid approach to track each source of plasma separately, which has the advantage
91 of allowing the plasma and the fields to evolve in a consistent manner. This technique can
92 use multiple continuity equations and a single momentum equation [*Glocer et al.*, 2009;
93 *Welling et al.*, 2011], or can involve multiple continuity, momentum, and energy equations
94 in a true multi-fluid MHD magnetosphere model [e.g., *Winglee et al.*, 2002; *Glocer et al.*,
95 2009; *Wiltberger et al.*, 2010].

96 While these previous approaches have advanced our knowledge of the effect of iono-
97 spheric plasma on the magnetosphere, they all suffer from significant shortcomings. Ide-
98 ally, a global model with an ionospheric source of plasma would include a separate solar
99 wind and polar wind proton population, a self-consistent ring current, and separate outflow
100 representations for each hemisphere. While some models in the literature include some
101 subset of these features, no model includes them all. Moreover, while there are global
102 magnetosphere models that include a cold dense plasmasphere population [e.g., *Zhang*
103 *et al.*, 2016; *Ouellette et al.*, 2016], or a ring current population [e.g., *De Zeeuw et al.*,
104 2004; *Glocer et al.*, 2013], there is not yet a published model that includes both of these
105 hot and cold populations simultaneously. This is a particularly troublesome problem as
106 the plasmasphere population carries much of the mass density in the inner magnetosphere,
107 whereas the ring current carries much of the energy density in the magnetosphere. Choos-
108 ing to only represent one population or the other means that significant physical effects
109 may go uncaptured.

110 In this paper we advance the current state-of-the-art by introducing new modeling
111 capabilities to address many of the shortcomings described above. The model presented
112 here builds on the recent work to separately track ionospheric and solar wind plasma
113 while simultaneously including hemispheric asymmetry in the outflow which is critical
114 to capturing seasonal effects. The model also includes a multi-component hot ring current
115 and cold plasmaspheric population in the global magnetosphere. We describe these ad-
116 vances in Section 2, and apply the model to a particular geomagnetic storm in Sections 3
117 and 4. Discussion of the results is given in Section 5.

2 Modeling Approach for Separating the Sources of Magnetospheric Plasma

The starting point for the modeling approach described in this paper is the configuration described by [Glocer *et al.*, 2018]. In that study, a multi-fluid MHD code (BATS-R-US) was combined with a fluid-kinetic outflow model (PWOM), and a bounce averaged kinetic ring current model (CIMI). These models are coupled together via the Space Weather Modeling Framework (SWMF), exchanging information at a frequent cadence [Tóth *et al.*, 2012]. This setup allows for a first principles representation of outflow, and the ability to track different plasma populations through the magnetosphere and into the ring current. We build on this set up by adding three new key features. First, the proton population is separated into solar wind and polar wind protons. Second, a separate plasmasphere fluid is included to enable the hot ring current and cold plasmasphere to both be represented in the inner magnetosphere. Finally, separate outflow solutions for the northern and southern hemispheres are included to allow for the study of hemispheric asymmetry of outflow on the magnetosphere. In the following subsections we provide a brief summary of each of the models used in the present study.

2.1 The Polar Wind Outflow Model (PWOM)

The Polar Wind Outflow Model (PWOM) [Glocer *et al.*, 2007, 2009] represents the high-latitude ionospheric source of plasma in this study. It provides a first principles calculation of ionospheric outflow, determining the solution of ionospheric H^+ , O^+ , He^+ and electrons in the transition region between the magnetosphere and ionosphere. The lower bound of the PWOM is located in the ionosphere below the F2 peak (altitude = 200 km), while the upper boundary is in the magnetosphere at a few Earth radii. The complete three dimensional solution is obtained by multiple field aligned solutions along field lines connecting through the polar cap. Recently, the model has been expanded to include a number of new features. These include the effect of superthermal electrons [Glocer *et al.*, 2012, 2017], as well as a transition to kinetic ions at high altitudes using a hybrid Macroscopic Particle-In-Cell (Mac-PIC) technique [Glocer *et al.*, 2018].

Superthermal electrons are critical to the modeling ionospheric outflow and were first added to PWOM by Glocer *et al.* [2012] with results found to be in excellent agreement with observations. Since that time a fully kinetic treatment of superthermal electrons has been added [Glocer *et al.*, 2017], as well as a two-stream representation [Glocer *et al.*, 2018] based on an adapted implementation of the GLOW code [Solomon *et al.*, 1988; Solomon, 2017]. In the present study we use the latter representation as an acceptable compromise between computational speed and including the appropriate physics.

The other recently added feature in PWOM used in this study is the inclusion of a kinetic treatment of ions [Glocer *et al.*, 2018]. Above the ion exobase located at about 2000km [Lemaire and Scherer, 1970], the validity of the hydrodynamic approach becomes increasingly suspect as there are few collisions to regularize the distribution function. Moreover, wave-particle interactions such as ion cyclotron heating, generate ion conics and other outflow distributions that are far from Maxwellian. PWOM can now treat these non-classical effects on the global outflow solution using a combined fluid-kinetic approach. Below 1000km, PWOM uses its original hydrodynamic approach to solve the gyrotropic transport equations for ions. Above 1000km, PWOM uses a hybrid PIC approach with Monte Carlo collisions to obtain a kinetic solution by following guiding center macro-particles for each ion species.

In our simulations where PWOM is coupled to the magnetosphere, we include both electron precipitation and wave-particle interactions. The electron precipitation in this simulation is based on the magnetospheric currents coming into the ionosphere and set according to empirical relationship described by Ridley *et al.* [2004]. The mean energy and energy flux of the precipitation is used to set the electron spectrum at the top of each PWOM field line and in particular sets the upper boundary of each instance of the GLOW

code associated with each field line. The associated superthermal electron transport, production, and energy deposition is thus included throughout the high latitude region as described in our previous studies [Glocer *et al.*, 2017, 2018]. For wave-particle interaction, we use the empirical heating terms provided by Barakat and Schunk [2001] in their equations 3 and 4 for both H⁺ and O⁺. As done in Glocer *et al.* [2018], we define a threshold of 1 erg/cm²/s to determine where to use wave-particle interaction terms appropriate to the cusp and aurora.

Beyond these recent advances, in this study we now account for separate outflow solutions in each hemisphere. Here we improved on an existing feature of PWOM that has not been often used. We know from observations that the outflow strength and composition have significant seasonal dependence [Lennartsson *et al.*, 2004]. However, our past modeling studies have only simulated outflow in the northern hemisphere and then assumed the same outflow for the southern hemisphere. By including a separate outflow calculation for each hemisphere, we are now able to study the the role of asymmetric outflow on the magnetosphere.

2.2 Multi-Fluid BATS-R-US

The Block-Adaptive-Tree Solar-wind Roe-type Upwind Scheme, or BATS-R-US, code is used to represent the magnetosphere in this paper. BATS-R-US is a truly multi-physics code capable of solving different equation sets in the magnetosphere including, MHD, Hall MHD [Tóth *et al.*, 2008], and anisotropic MHD [Meng *et al.*, 2012]. Of particular relevance to this study is the ability to solve the multi-fluid MHD equations given by [Glocer *et al.*, 2009]:

$$\frac{\partial \rho_s}{\partial t} + \nabla \cdot (\rho_s \mathbf{u}_s) = S_{\rho_s} \quad (1)$$

$$\frac{\partial \rho_s \mathbf{u}_s}{\partial t} + \nabla \cdot (\rho_s \mathbf{u}_s \mathbf{u}_s + I p_s) = n_s q_s (\mathbf{u}_s - \mathbf{u}_+) \times \mathbf{B} + \frac{n_s q_s}{n_e e} (\mathbf{J} \times \mathbf{B} - \nabla p_e) + S_{\rho_s \mathbf{u}_s} \quad (2)$$

$$\frac{\partial p_s}{\partial t} + \nabla \cdot (p_s \mathbf{u}_s) = -(\gamma_s - 1) p_s \nabla \cdot \mathbf{u}_s + S_{p_s} \quad (3)$$

$$\frac{\partial \mathbf{B}}{\partial t} - \nabla \times (\mathbf{u}_+ \times \mathbf{B}) = 0 \quad (4)$$

$$\frac{\partial p_e}{\partial t} + \nabla \cdot (p_e \mathbf{u}_e) = -(\gamma_e - 1) p_e \nabla \cdot \mathbf{u}_e + S_{p_e} \quad (5)$$

where γ_s adiabatic index for ion, and γ_e is the adiabatic index for electrons. The s and e subscripts represent the ion or electron fluids respectively. Other variables include the ion (q_s) and electron (e) charge densities, the number density (n), mass density (ρ), velocity (\mathbf{u}), pressure (p), current density (\mathbf{J}), magnetic field (\mathbf{B}), and source terms (S) whose subscript indicates the type. \mathbf{u}_+ represents the charge averaged ion velocity defined by the following:

$$\mathbf{u}_+ = \frac{\sum_s n_s q_s \mathbf{u}_s}{en_e} \quad (6)$$

Where n_e is the total electron number density set equal to the sum of the ion number density due to quasineutrality. In these simulations we set the electron velocity $u_e = u_+$, so the Hall effect is neglected. Note that source term (S_{ρ_s}) representing mass exchange as a result of chemical processes are included here for completeness, but are set to zero for this study. On the other hand, a momentum source term ($S_{\rho_s \mathbf{u}_s}$) is included to limit the velocity difference parallel to the magnetic field line and represent the effect of streaming instabilities. This term is described by [Glocer *et al.*, 2009] and takes the form of an artificial friction term given by:

$$S_{\rho \mathbf{u}_s}^{friction} = \frac{1}{\tau_c} \sum_{q \neq s} \min(\rho_s, \rho_q) (\mathbf{u}_q - \mathbf{u}_s) \left(\frac{|\mathbf{u}_s - \mathbf{u}_q|}{u_c} \right)^{\alpha_c} \quad (7)$$

where q indexes all the other fluids, τ_c is the *cut-off* time scale, u_c is the cut-off velocity and α_c is the cut-off exponent. We choose to limit the relative ion velocities parallel to the magnetic field to the local Alfvén speed as done in [Opher et al., 2020].

In this paper we advance the multi-fluid treatment presented in [Glocer et al., 2009] in two straight forward but important ways. First, we expand the number of fluids considered to allow for the inclusion of separate H^+ fluids from the high latitude ionosphere (polar wind) and solar wind as well as a separate plasmasphere fluid. This is an improvement over the treatment in [Glocer et al., 2009] which only had two ion fluids (H^+ and O^+). It also builds on the recent work showing the advantages of separating the solar wind and ionospheric H^+ populations. Second, we expanded the coupling between BATS-R-US and CIMI, and BAT-R-US and PWOM, to take advantage of these additional fluids.

2.3 Comprehensive Inner Magnetosphere Ionosphere (CIMI) Model

To model the ring current we will be using the Comprehensive Inner Magnetosphere-Ionosphere (CIMI) model [Fok et al., 2014]. The CIMI model is a kinetic model that combines the Comprehensive Ring Current Model (CRCM) [Fok et al., 2001] and the Radiation Belt Environment (RBE) model [Fok et al., 2011] to obtain energetic ion (0.1 keV - 400 keV) and electron (1 keV - 4 MeV) distributions, plasmaspheric densities. In the version of CIMI coupled with the Space Weather Modeling Framework (SWMF) we are solving the bounce-averaged Boltzmann equation for the distribution functions of ring current-radiation belt particles given as follows:

$$\begin{aligned} \frac{\partial f_s}{\partial t} + \langle \dot{\lambda}_i \rangle \frac{\partial f_s}{\partial \lambda_i} + \langle \dot{\phi}_i \rangle \frac{\partial f_s}{\partial \phi_i} &= \frac{1}{G} \frac{\partial}{\partial \alpha_0} \left[G \left(D_{\alpha_0 \alpha_0} \frac{\partial f_s}{\partial \alpha_0} + D_{\alpha_0 E} \frac{\partial f_s}{\partial E} \right) \right] \\ &+ \frac{1}{G} \frac{\partial}{\partial E} \left[G \left(D_{EE} \frac{\partial f_s}{\partial E} + D_{E \alpha_0} \frac{\partial f_s}{\partial \alpha_0} \right) \right] - \nu \sigma_{sH} \langle n_H \rangle f_s - \left(\frac{f_s}{0.5 \tau_b} \right)_{losscone} \end{aligned} \quad (8)$$

where $G = T(\alpha_0) \sin 2\alpha_0 (E + E_0) \sqrt{E(E + 2E_0)}$. $f_s = f_s(t, \lambda_i, \phi_i, M, K)$ is defined by the average of the distribution function between mirror points of a given field line. The magnetic latitude (λ_i) and local time (ϕ_i) are both defined at the ionospheric foot point of the geomagnetic field line. M is the relativistic magnetic moment, and $K = J/\sqrt{8m_0 M}$ where J is the second adiabatic invariant. Particles motion is described by their drifts across field lines and calculated at ionospheric foot points. The rest energy is given by E_0 and α_0 represents the equatorial pitch angle. $T(\alpha_0)$ is a function depending on α_0 and the shape of the field line.

The left hand side of equation 8 represents the drifts of the particle population, while the right hand side represents source and loss terms due to wave-particle interactions, charge exchange, and the loss cone. The drifts include the gradient-curvature drift, $E \times B$ drift from convection, as well as co-rotation. Note that the convection electric field is passed to CIMI from the SWMF and represents the electrodynamics coupling between the ionosphere and the magnetosphere. The effects of the inductive electric field due to a time-varying magnetic field are also taken into account implicitly in the model [Keller et al., 2005]. In this study, our main focus is on the ring current ions and thus we ignore VLF wave-particle interactions by setting wave diffusion coefficients in energy (D_{EE}), angle ($D_{\alpha_0 \alpha_0}$), and mixed ($D_{\alpha_0 E}$) to zero. They are included here, however, for completeness as they are available in the model. The second to last terms on the right hand side of Equation 8 represents the charge exchange loss for ions where σ_{sH} is the charge exchange cross section for a species 's' with hydrogen in the geocorona. The final term on the right hand side of Equation 8 represents the loss cone loss with a half bounce period lifetime.

Critical to the the present study is the inclusion of a separate plasmasphere fluid in the multi-fluid BATS-R-US code. That fluid is filled entirely from the CIMI code based

249 on it's embedded core plasmasphere model. That model solves an equation for the total
250 plasmasphere ion content (N) per unit magnetic flux according the following equation:

$$\frac{\partial N}{\partial t} + \langle \lambda_i \rangle \frac{\partial N}{\partial \lambda_i} + \langle \phi_i \rangle \frac{\partial N}{\partial \phi_i} = \frac{F_n + F_s}{B_i} \quad (9)$$

251 where F_N and F_S are empirical refilling rates for the northern and southern hemispheres.
252 The plasmasphere model calculates plasmaspheric density distribution considering co-
253 rotation, convection, daytime refilling, and night side diffusion [Fok *et al.*, 2005]. These
254 densities are then fed back to BATS-R-US to populate the plasmasphere fluid with two
255 important assumptions. First, this type of plasmasphere model does not have informa-
256 tion regarding the density distribution along the field line. We therefore make the simplest
257 assumption that the average density is constant along the field line. Second, this type of
258 plasmasphere model does not specify the plasmasphere temperature or pressure. We there-
259 fore assume a temperature of 1eV and then hold the pressure fixed along the field line.
260 These assumptions can be relaxed in the future as new plasmasphere representations be-
261 come available in CIMI, but they suffice for the present study.

262 3 Case Study: The 6-7 June 2013 Event

263 In this paper we aim to illustrate the importance of three issues: (1) The relative
264 importance of solar wind and ionospheric protons, (2) the impact of hemispheric asym-
265 metry of outflow on magnetospheric composition, and (3) the impact of the plasmasphere
266 on the global magnetospheric solution. To that end we apply our model described in the
267 previous section, to the particular event of 6-7 June 2013. This is a modest event with a
268 maximum Kp index of 6 and minimum Dst of -78 nT. The F10.7 value of 110 indicates
269 that the solar EUV flux input is also modest, although there is a significant seasonal asym-
270 metry in illumination. The solar wind conditions upstream of the magnetosphere are given
271 in Figure 1. Our simulation time goes from just before the large southward Bz turning on
272 6 June, and runs for approximately 1 day. In order to examine the effect of the plasma-
273 sphere, we conduct this simulation both with a very full plasmasphere and without any
274 plasmasphere. These two cases represent limiting scenarios that enable us to examine the
275 maximum extent of plasmaspheric impacts on the system. In each case, we are able sep-
276 arate the relative contribution of O^+ as well as solar wind and ionospheric protons to the
277 magnetosphere and into the ring current.

279 We begin our analysis by examining the outflow solution during the storm. Figure
280 2, shows a map of the outflow fluxes of O^+ and H^+ during the main phase of the event
281 for both the northern and southern hemispheres. Each panel is a slice at a constant alti-
282 tude of 6,000km with the sun-ward direction towards the top of the plot. The location
283 of the field-line foot-points in the simulation at this time are indicated by the white '+'
284 symbols. The overall outflow flux for both H^+ and O^+ is stronger in the northern summer
285 hemisphere and weaker in the southern winter hemisphere. However, the effect is more
286 strongly seen in the O^+ flux that exhibits a much stronger seasonal dependence. We find
287 that the H^+ flux is generally spread out over the sunlit high latitude region, which covers
288 a larger portion of the northern hemisphere than the southern hemisphere. The O^+ flux, in
289 contrast, is organized more around the auroral zone and cusp. Additionally, there is a pro-
290 nounced downward shift from noon of the O^+ flux at this time. At later times in the event
291 (not shown) the shift becomes less obvious or even disappears. As discussed by *Redmon*
292 *et al.* [2012], observations indicate that a dawnward shift in the peak dayside O^+ flux is
293 expected during low activity periods, but the shift can disappear during active times.

294 In terms of the overall fluxes we note that the values shown are reasonable as com-
295 pared to observations. In Figure 2 we find the H^+ fluxes to be on the order of $10^7 \text{ cm}^{-2}\text{s}^{-1}$
296 at 6,000 km. That value corresponds well with observed values of the polar wind. For in-
297 stance, *Hoffman and Dodson* [1980] reported observations of polar wind fluxes from the
298 Isis 2 satellite on the order of $10^8 \text{ cm}^{-2}\text{s}^{-1}$ at 1,400 km which corresponds to a flux of

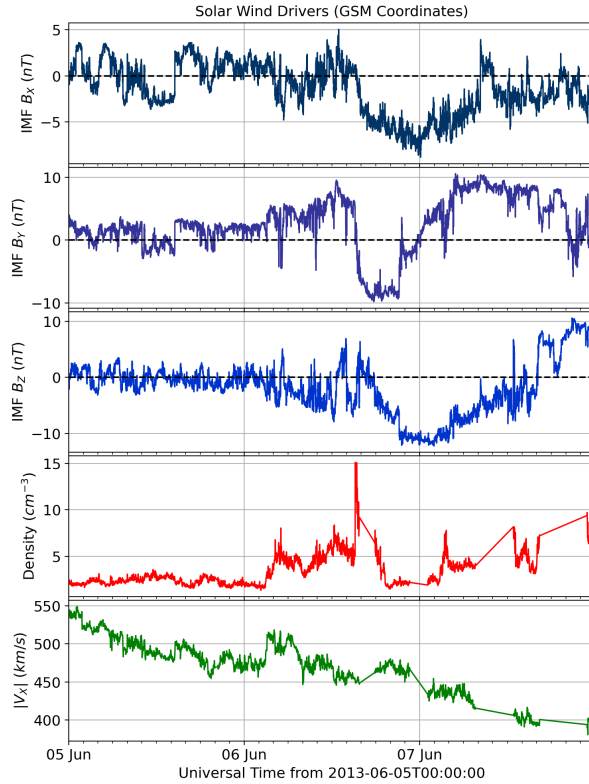


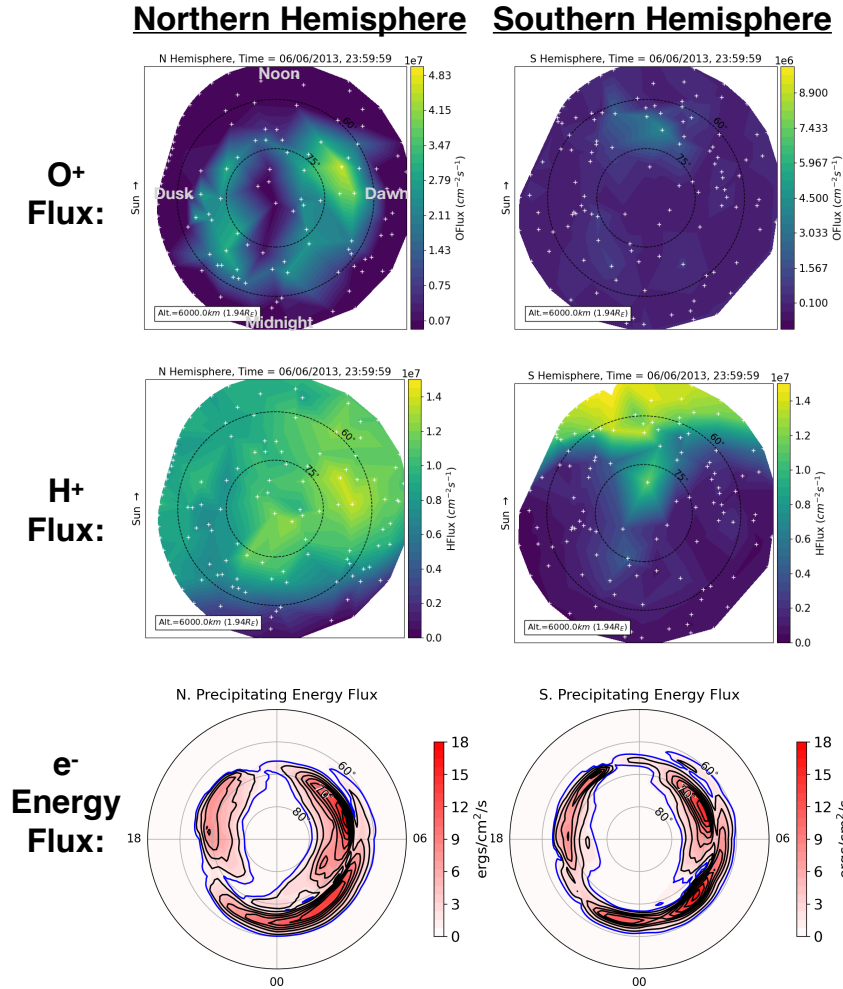
Figure 1. Solar wind conditions during the 6-7 June 2013 event from the ACE satellite.

278

299 about $2.5 \times 10^7 \text{ cm}^{-2}\text{s}^{-1}$ at 6,000 km. Similar values of $6.0 \times 10^7 \text{ cm}^{-2}\text{s}^{-1}$ at 5,000 km are
 300 reported by *Huddleston et al.* [2005] from Polar spacecraft observations. Therefore, our
 301 modeled H^+ fluxes are on the same order, if somewhat less than observed levels. In con-
 302 trast, it is harder to estimate the reasonableness of the O^+ fluxes which observations have
 303 shown to be highly variable and depend strongly on the energization. Indeed, observations
 304 from the Fast Auroral SnapshoT (FAST) satellite shows accelerated O^+ fluxes anywhere
 305 between $10^5 \text{ cm}^{-2}\text{s}^{-1}$ and $10^9 \text{ cm}^{-2}\text{s}^{-1}$ at about 4,000 km [*Zhao et al.*, 2020; *Strangeway*
 306 *et al.*, 2005]. Our peak fluxes, on the order of $4.0 \times 10^7 \text{ cm}^{-2}\text{s}^{-1}$, fall within the range of
 307 past observations, but no stronger claim can be made without more available data.

308 It also is interesting to evaluate the role of asymmetry in the precipitation as a pos-
 309 sible contributor to the asymmetry in the outflow flux. We therefore include the precipitat-
 310 ing electron energy flux in each hemisphere in the bottom row of Figure 2. While there
 311 are modest differences in the precipitation patterns between the northern and southern
 312 hemispheres, the two precipitating distributions are qualitatively similar. Moreover, as
 313 the wave-particle interactions in the auroral region are applied in the model by evaluat-
 314 ing when the energy flux crosses a threshold of $1 \text{ erg/cm}^2/\text{s}$ (see Section 2.1) as indicated
 315 by the blue contour line, comparable wave-heating is specified in each hemisphere. As a
 316 result, we do not believe asymmetric auroral precipitation has a significant contribution to
 317 the hemispheric asymmetry of the outflow in our simulation.

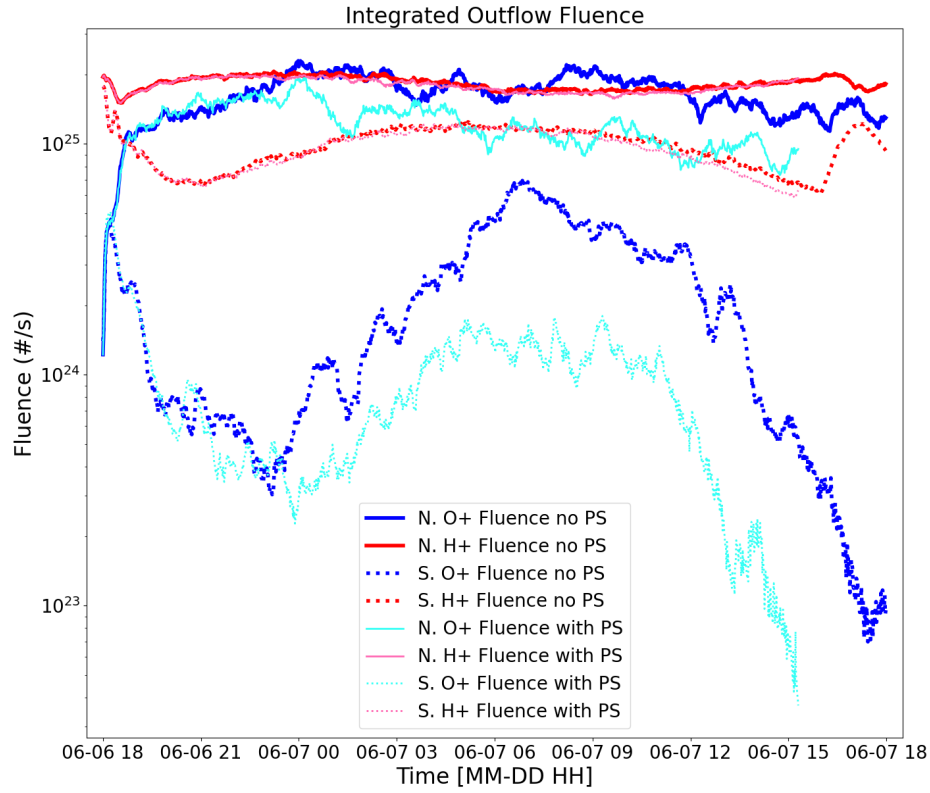
318 To make the outflow solution more quantitative, we calculate the net fluence, defined
 319 by the number of particles coming out of each hemisphere at each time in our simulations.
 320 To compute this value, we extract the solution each minute at 6,000 km that is near the
 321 top of the simulation domain. That extracted solution is on an unstructured grid defined
 322 by the field-line locations at each time. We interpolate the solution from the unstructured



325 **Figure 2.** The outflowing ion fluxes during the main phase of the storm illustrating the hemispheric asym-
 326 metry of the outflow. The northern (left column) and southern (right column) hemispheres are shown for O⁺
 327 (top row) and H⁺ (middle row). Note that the O⁺ flux in the southern hemisphere has the peak of the color
 328 bar reduced by approximately a factor of 5 to compensate for the much weaker outflow. The case without
 329 plasmasphere is shown. The white '+' symbols denote the location of the field-line foot points in the simu-
 330 lation. The bottom row shows the electron precipitating energy flux at this time at an altitude of 110 km. The
 331 blue contour corresponds to 1 erg/cm²/s. All latitudes in this figure are invariant latitudes.

323 grid onto a regular spherical grid and integrate the number flux times the area element to
 324 obtain fluence for O⁺ and H⁺ at each time.

332 Figure 3 presents the net fluences of O⁺ and H⁺ particles coming out of each hemi-
 333 sphere for simulations with and without a plasmasphere included. Similar to the results
 334 shown in Figure 2, we see a strong seasonal asymmetry in the outflow solution with more
 335 H⁺ and O⁺ outflow in the northern summer hemisphere and less in the southern winter
 336 hemisphere. Additionally, the seasonal asymmetry is more pronounced for O⁺ than for
 337 H⁺. Figure 3, further demonstrates that the inclusion of a plasmasphere in the magne-
 338 toospheric solution suppresses the O⁺ outflow and changes the composition of the total
 339 outflow. Specifically, when a plasmasphere is included, the fluence O⁺ decreases and the

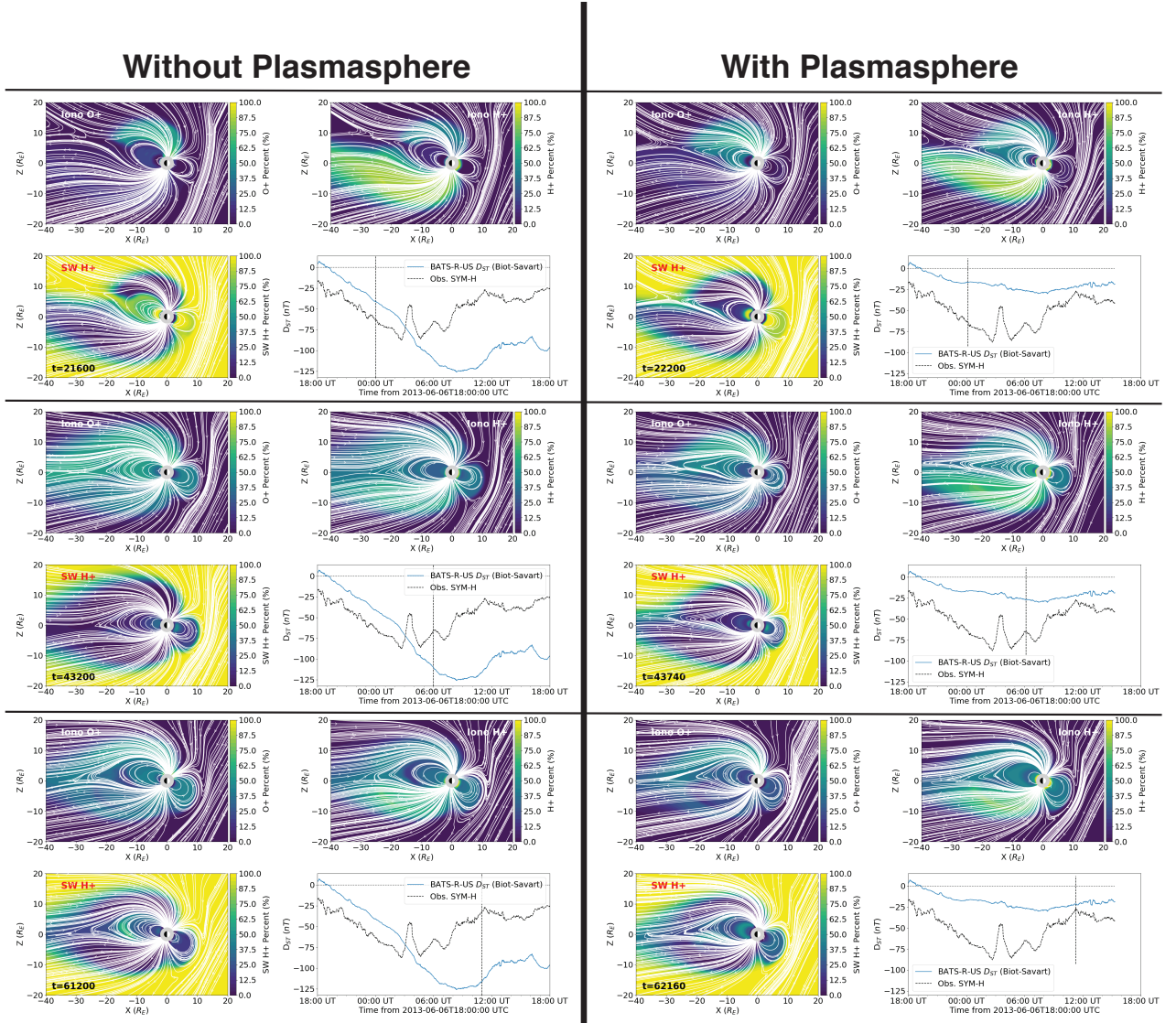


342 **Figure 3.** The integrated fluence of O^+ (blue/cyan line) and H^+ (red/pink line) particles coming out of the
 343 northern (solid line) and southern (dotted line) hemispheres. The solution is shown both without (thick line)
 344 and with (thin line) an included plasmasphere. We see stronger outflow in the northern summer hemisphere,
 345 and that the inclusion of a plasmasphere suppresses the O^+ outflow.

340 outflow composition contains a higher proportion of H^+ and a lower proportion of O^+ .
 341 Possible reasons for this plasmaspheric impact will be discussed later.

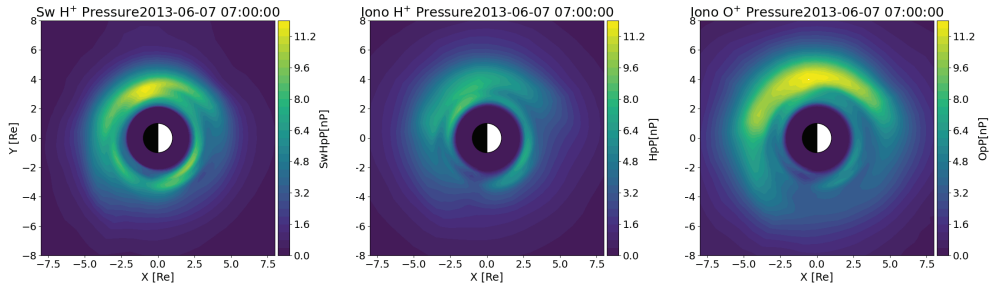
346 The hemispheric asymmetry seen in the outflow solution is manifest in the magne-
 347 tosphere. Figure 4 presents the evolution of magnetospheric composition with and without
 348 plasmasphere. Three time periods are shown, the storm main phase, the storm peak, and
 349 during the early recovery. Each panel of the figure shows $y=0$ GSM plane at a particular
 350 time with color contours representing the percentage of plasma contributed by each con-
 351 stituent species. These include ionospheric O^+ and H^+ as well as solar wind H^+ . Note
 352 that for this comparison we do not include the plasmasphere fluid in the percentage calcu-
 353 lation. We find that in both simulations the asymmetry in the outflow solution translates
 354 into asymmetric composition in the lobes. Specifically, we find that the northern lobe has
 355 a higher percentage of O^+ than the southern lobe, and the southern lobe is mostly popu-
 356 lated by polar wind protons. Interestingly, composition asymmetry can at times persist all
 357 the way to the x-line in the tail, resulting in asymmetry in composition on either side of
 358 the x-line.

363 The evolution of the magnetosphere from one whose plasma mostly comes from the
 364 solar wind to one whose plasma mostly comes from the ionosphere is also evident in Fig-

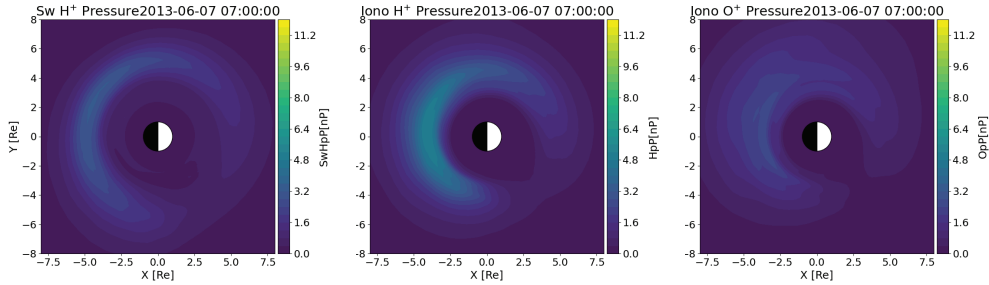


359 **Figure 4.** The evolution of the magnetospheric composition without plasmasphere (left column) and with
 360 plasmasphere (right column). Each panel has three color contour plots in the $y=0$ GSM plane showing the
 361 percentage of plasma from each source, excluding the plasmasphere fluid. Each panel also has a comparison
 362 of the simulated Dst with observations with vertical dashed line indicating the time shown in the panel.

Ring Current Pressure Without Plasmasphere



Ring Current Pressure With Plasmasphere

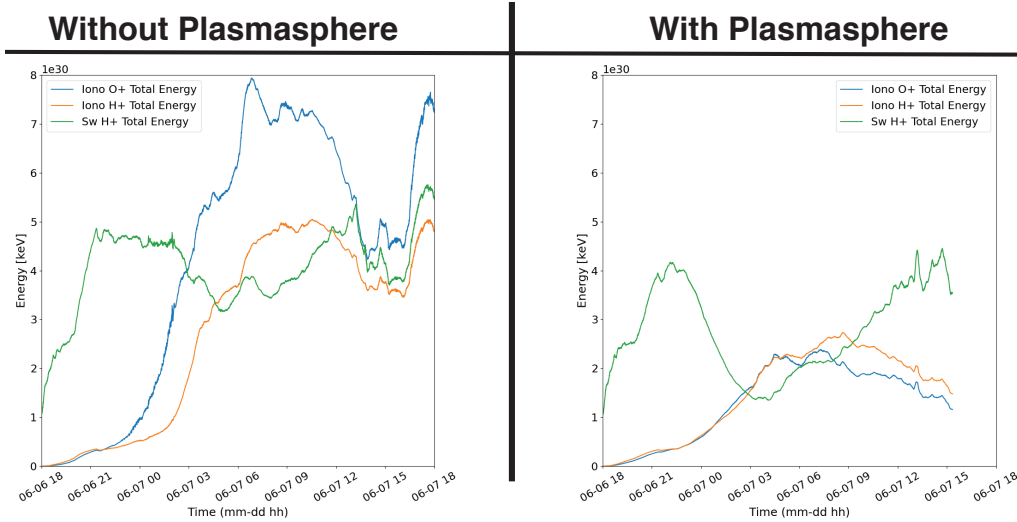


376 **Figure 5.** The ring current pressure near the peak of the storm for solar wind H^+ (left), ionospheric H^+ , and
 377 ionospheric O^+ . Results are shown without a plasmasphere included (top) and with a plasmasphere included
 378 (bottom).

385 ure 4. Our simulation starts with only solar wind plasma, but during the main phase of
 386 the storm much of the solar wind is flushed out of the plasmasheet and is largely replaced
 387 with ionospheric H^+ and O^+ . This change in composition is substantial, but not perma-
 388 nent. During the early recovery, additional solar wind H^+ gets re-injected into the plas-
 389 masheet and solar wind protons begin to slowly reestablish their contribution to the plas-
 390 masheet. While the story is largely similar regardless of whether plasmasphere is included
 391 or not, there are some differences. For example, the solar wind protons get displaced more
 392 rapidly when the plasmasphere is included, and the calculated Dst index is much lower
 393 without the plasmasphere indicating a more intense ring current. Both effects are likely
 394 due to a reduction of efficiency in the solar wind - magnetosphere coupling when a plas-
 395 masphere is included which will be further discussed later in this section.

396 Moving inward from the plasmasheet we shift our focus to the ring current solution.
 397 Figure 5 presents the ring current pressure from the CIMI model on the surface defined
 398 by the minimum of the magnetic field at a time near the storm peak. Pressure values are
 399 shown for solar wind and ionospheric protons as well as ionospheric O^+ . We find that
 400 the ring current pressure in each species is strongly reduced when the plasmasphere is
 401 included. In the case when no plasmasphere is included the O^+ is the dominant contribu-
 402 tor to the pressure followed by the solar wind protons and then protons of ionospheric
 403 origin. Additionally, multiple ring current injections occur when examining a time series
 404 of simulation output (not shown). When including the plasmasphere, the ring current is
 405 less dynamic with fewer injections. Moreover, H^+ of ionospheric origin is found to be the
 406 largest contributor to the ring current pressure at this time.

407 To understand how different plasma sources contribute to the ring current over time,
 408 it is useful to examine the total ring current energy carried by each constituent. We do
 409 this by integrating over phase space at each time to obtain the total energy carried by solar
 410 wind.

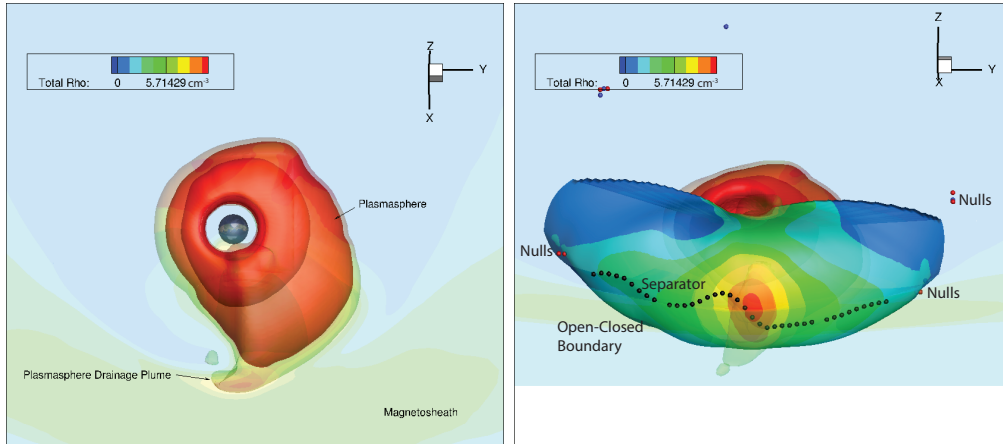


406 **Figure 6.** Total energy content in the ring current by species as a function of time when a plasmasphere is
 407 not included (left) and when a plasmasphere is included (right).

393 wind H^+ , ionospheric H^+ , and ionospheric O^+ . That time series is presented in Figure 6.
 394 When the plasmasphere is not included, O^+ carries most of the energy density from the
 395 peak of the storm until the end of the simulation. The solar wind and ionospheric H^+ be-
 396 come roughly equal contributors to the ring current energy during this period. When the
 397 plasmasphere is included the overall energy in the ring current is sharply reduced. Dur-
 398 ing the peak of the storm the ionosphere briefly becomes the main contributor to the ring
 399 current plasma, but later in the simulation the solar wind and ionospheric contributions
 400 become roughly equal (summing ionospheric species together). Interestingly, if one were
 401 to assume that all protons came from the solar wind, as is often the case, then in both
 402 simulations the solar wind would be the dominant contributor to the ring current energy.
 403 However, by separating the solar wind and ionospheric protons into two populations it is
 404 clear that the ionosphere contributes a major portion of the ring current in both simula-
 405 tions for this fairly moderate event.

408 Thus far in this section, we have found that the plasmasphere as we have modeled
 409 it can have a profound impact on the entire magnetosphere. Our hypothesis for this effect
 410 is that the initially very full plasmasphere forms a drainage plume during the storm main
 411 phase that then creates a region of very high density at the dayside magnetopause. Cold
 412 dense plasma near the reconnection site drives the dayside reconnection rate down as in-
 413 dicated by prior studies [Borovsky and Steinberg, 2006; Ouellette et al., 2016; Walsh et al.,
 414 2014]. As the reconnection rate is reduced, the effectiveness of the transfer of energy from
 415 the solar wind to the magnetosphere is also decreased. The reduction in the coupling effi-
 416 ciency has a system wide effect. It reduces the outflow and changes the composition of
 417 the ionospheric plasma entering the magnetosphere, slows the convection in the magne-
 418 totail, reduces the build up of the ring current, and impacts magnetospheric composition.
 419 This is the first time such a system wide impact due to the plasmasphere has been demon-
 420 strated in either simulation or observations.

421 To test our hypothesis we examine the location of the density increase at the day-
 422 side magnetopause relative to the reconnection separator line, and then the impact on so-
 423 lar wind - magnetosphere coupling. Figure 7 shows a three dimensional representation of
 424 the plasmasphere using isosurfaces of constant density. The figure also shows the open-
 425 closed field line boundary with the total mass density painted on the surface, and the mag-



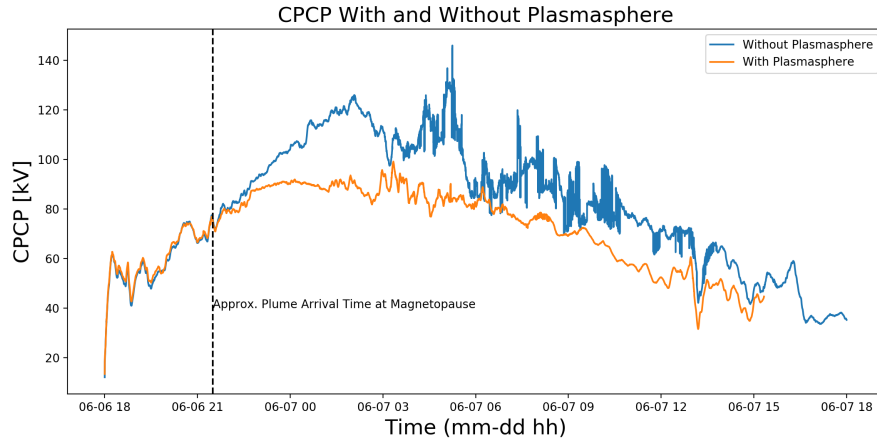
435 **Figure 7.** 3D representation of the plasmasphere plume (shown as isosurfaces), encountering the open-
 436 closed field line boundary. Two perspectives are shown: top down and upstream of the magnetosphere. The
 437 magnetic separator is indicated by the black dots, and the nulls by the colored dots. The time is 4 hours into
 438 the simulation, or about 30 minutes after the initial plume arrival at the magnetopause.

426 netic separator extracted using the technique described in *Glocer et al.* [2016]. The density
 427 on the dayside magnetopause is strongly enhanced in the vicinity of the separator, the
 428 line along which reconnection is occurring. We note that the density of the plume near
 429 the magnetopause, on the order of 10 cm^{-3} , is reasonable compared with typical space-
 430 craft observations of plasmapheric drainage plumes [e.g., *Walsh et al.*, 2013; *Lee and An-*
 431 *gelopoulos*, 2014; *Lee et al.*, 2016]. It is also interesting to note that the separator exhibits
 432 a twist at the location that the plume encounters the magnetopause. The enhanced den-
 433 sity at the separator is expected to reduce the reconnection rate and the convection in the
 434 magnetosphere.

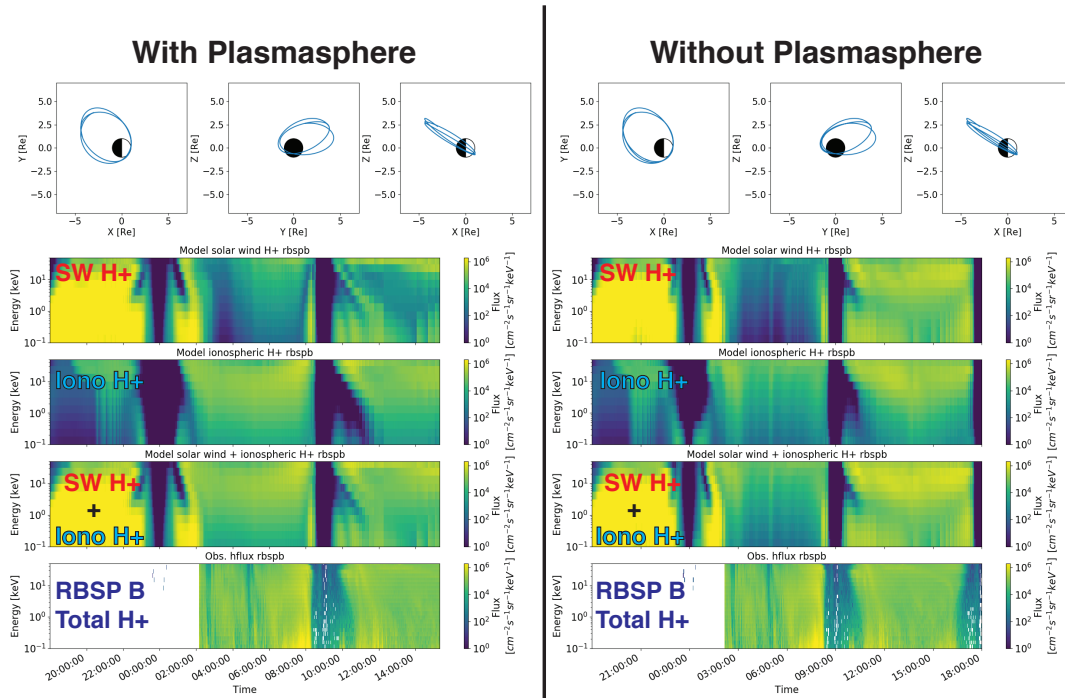
439 Evidence of the reduced coupling of the solar wind energy into the magnetosphere
 440 is found when looking at the cross polar cap potential. Figure 8 compares the cross po-
 441 lar cap potential in the northern hemisphere for cases without and with a plasmasphere
 442 included. The approximate arrival time of the plume at the magnetopause is indicated by
 443 the vertical dashed line in the plot. Prior to the plume arrival at the magnetopause the two
 444 simulations are remarkably similar. However, after the plume arrival, the two solutions
 445 begin to diverge significantly. The simulation with a plasmasphere exhibits a lower cross
 446 polar cap potential than the simulation without a plasmasphere. The reduced polar cap
 447 potential is indicative of reduced energy input to the magnetosphere, which is likely the
 448 cause of the reduced convection and other systematic changes seen in our simulations.

452 **4 Comparison with Van Allen Probe Data**

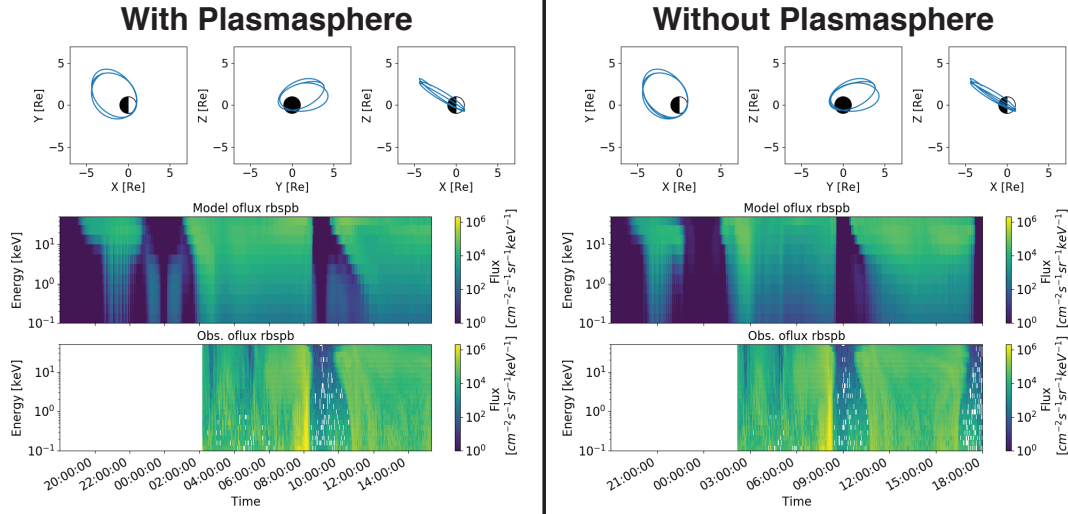
453 In the prior section we found a number of interesting features in the simulation in
 454 terms of the relative contribution of different sources of plasma, the role of hemispheric
 455 asymmetry of outflow, and the system-wide impact of including the plasmasphere. How-
 456 ever, the only data-model comparison included thus far has been with the Dst index, which
 457 is a good overall measure of ring current intensity, but lacks composition information.
 458 Fortunately, Van Allen Probe (RBSP) data of ion composition from the HOPE instrument
 459 is available from the peak of the storm onward. While perfectly fitting the observations is
 460 not an objective of this study, comparison with the observations can yield some guidance
 461 on the overall reasonableness of the simulations.



449 **Figure 8.** The temporal evolution of the cross polar cap potential (CPCP) in the northern hemisphere
 450 without (blue) and with (orange) a plasmasphere included. Note that the plume arrives at the magnetopause
 451 approximately 3.5 hours into the simulation.



462 **Figure 9.** Comparison of simulated and observed H^+ ion spectra along the RBSP B satellite trajectory
 463 starting on 6 June and ending on 7 June. The orbit is shown in the top panel, the first and second row of spectra
 464 represent the simulated solar wind and ionospheric H^+ respectively. The third row of spectra presents the
 465 total solar wind and ionospheric H^+ . The total observed H^+ is shown on the bottom. The simulation with
 466 plasmasphere is on the left and the simulation without plasmasphere is on the right.



495 **Figure 10.** Comparison of simulated and observed O^+ ion spectra along the RBSP B satellite trajectory
 496 starting on 6 June and ending on 7 June. The orbit is shown in the top panel, the top spectra represent the
 497 ionospheric O^+ . The observed O^+ is shown on the bottom. The simulation with plasmasphere is on the left
 498 and the simulation without plasmasphere is on the right.

467 Figure 9 presents the comparison of the simulated and observed proton spectra along
 468 the RBSP B satellite trajectory. As RBSP A and B are in very similar orbits at this time,
 469 we only present the comparison with one satellite and simply note that similar results are
 470 found for each satellite. We extract synthetic spectra of solar wind and ionospheric H^+
 471 from the CIMI portion of the coupled model using the technique described in *Glocer et al.*
 472 [2013]. Those results are compared with the observed proton spectra from HOPE, which
 473 necessarily represents the total proton solution from every source. From the comparison
 474 of the simulated and observed spectra, we note the following. First, we find that at the
 475 peak of the storm protons of ionospheric origin are able to account for much of the ob-
 476 served protons in the HOPE energy range. But towards the end of the simulation both
 477 ionospheric and solar wind proton sources become important again. Second, the overall
 478 intensity of the observed and simulated spectra are comparable and some similarity of fea-
 479 tures is evident indicating a qualitative agreement. Moreover, summing up the solar wind
 480 and ionospheric protons gives a better qualitative comparison to the observations indicat-
 481 ing that both sources of protons are required to adequately understand protons in the ring
 482 current. Finally, we note that the simulation with plasmasphere has protons of ionospheric
 483 origin playing a somewhat more prominent role as compared to the simulation without a
 484 plasmasphere included. This is consistent with our analysis of the ring current energy in
 485 the previous section that found ionospheric H^+ carries more ring current pressure in the
 486 simulation when a plasmasphere is included.

487 Figure 10 presents the comparison of the simulated and observed O^+ spectra along
 488 the RBSP B satellite trajectory. Again the overall intensity of the simulated and observed
 489 spectra are similar as are some of the features indicating a qualitative agreement. We note
 490 that when the plasmasphere is included there appears to be more O^+ in the simulated
 491 HOPE energy range as the simulation without a plasmasphere has a hotter population
 492 shifting part of the flux to higher energies. Additionally, the simulation with a plasmas-
 493 phere appears smoother near the peak of the storm (3-7UT) than the case without a plas-
 494 masphere, consistent with this simulation showing fewer O^+ injections.

Clearly there is a strong difference seen when including a plasmasphere, but it is important to note that we are focusing on two limiting cases: no plasmasphere and very full plasmasphere. No attempt was made to initialize with the observed values. Instead we use these limiting cases to establish the impact the plasmasphere may have on the system. Comparison of the simulated plasmasphere with the observed total electron density from EMFISIS (not shown), indicates reasonable agreement inside of the plasmopause but that the simulated plasmopause extends further out than is observed. This is entirely due to the initial condition and is intentional.

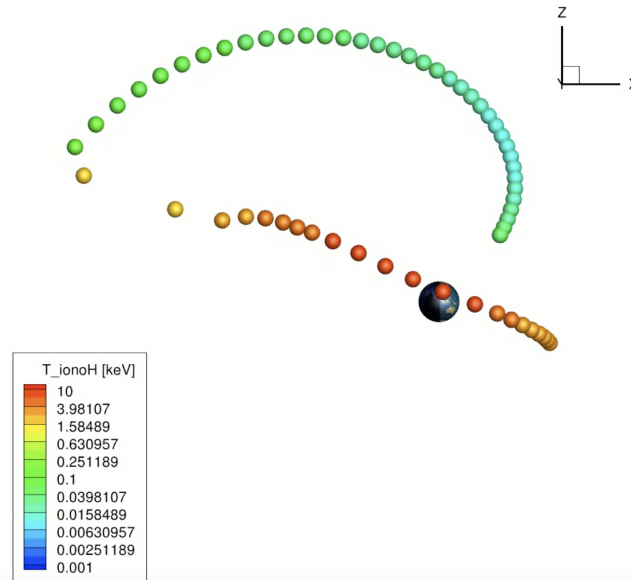
5 Discussion and Conclusions

In this study we focused on three issues: the relative contribution of ionospheric and solar wind protons during a storm, the hemispheric asymmetry of outflow and its consequences for the magnetosphere, and the system-wide impact of the plasmasphere. To enable this study we use the SWMF to couple models of ionospheric outflow (PWOM), the global magnetosphere (BATS-R-US), the ionosphere electrodynamics, and an embedded inner magnetosphere model (CIMI) as described by *Glocer et al.* [2018] with some key improvements including the option of including a plasmasphere model. For the remainder of this section we will summarize and discuss the modeling advancements and scientific findings of our study.

The key modeling enhancements we introduce relative to the model described in *Glocer et al.* [2018] include adding the ability to separately track ionospheric and solar wind protons in the magnetosphere (building on recent work), including separate outflow representations for each hemisphere, and including a separate cold plasmasphere fluid in the magnetosphere. While new to our modeling studies, the first two features are present to some degree in previous studies. For instance, separation of solar wind and ionospheric protons was included in the test particle modes like *Moore et al.* [2005], but without a first principles model of ion outflow. The separation of proton sources is also included in the fluid model of [Varney et al., 2016], but without separate northern and southern hemisphere ion outflow solutions. Similarly, hemispheric asymmetries of outflow are examined in the first principles outflow model of *Schunk and Sojka* [1997], but no coupling of the outflow into the magnetosphere is included. The present model, represents a tangible step forward in that it includes a first principles model of ionospheric outflow coupled to the magnetosphere, with hemispheric asymmetry, and separate fluids for the solar wind and ionospheric protons.

Including cold plasmasphere and hot ring current populations simultaneously in a global magnetosphere model is likewise a significant advance. When a typical single fluid global magnetosphere model is coupled to an inner magnetosphere model [e.g., *De Zeeuw et al.*, 2004; *Glocer et al.*, 2013; *Meng et al.*, 2013] a choice typically has to be made as to whether to represent the plasmasphere which carries the majority of the density or the ring current which carries the pressure. This is because the distribution function underpinning a typical single fluid MHD model cannot simultaneously represent the cold and hot populations simultaneously. The advent of multi-fluid magnetospheric models, however, make it possible to couple the hot and cold populations to separate fluids. Nevertheless, until now multi-fluid codes have either included a plasmasphere without a ring current model [e.g., *Zhang et al.*, 2016; *Ouellette et al.*, 2016], or a ring current without a plasmasphere [*Glocer et al.*, 2018]. In the present work we allow an inner magnetosphere model, CIMI, to advance the ring current and plasmasphere solutions in the inner magnetosphere while fully coupled to the multi-fluid BATS-R-US magnetosphere model. In this way a multi-component hot ring current and cold plasmasphere can be included simultaneously in the global magnetosphere for the first time.

When the modeling advances described above were applied to the geomagnetic storm of 6-7 June 2013, we found that ionospheric protons play a major role in populating



563 **Figure 11.** In this figure we are showing “particles” following the ionospheric H^+ fluid velocity near 5UT.
 564 The particles are launched above the MHD inner boundary and flow back to the tail where they are brought
 565 earthward by the cross tail convection electric field. The particles are colored by the the ionospheric H^+ tem-
 566 perature showing how the initially cold ionospheric population is accelerated to plasmashet and warm plasma
 567 cloak temperatures.

550 the magnetosphere. During the storm main phase and peak, protons of ionospheric ori-
 551 gin make up a major portion of the plasmashet, displacing much of the solar wind proton
 552 contribution. Similarly, ionospheric protons comprise a significant portion of the ring cur-
 553 rent pressure during this time. Later in the simulation, solar wind protons start to build
 554 up again in the plasmashet and ring current due to new injections from the tail. Just how
 555 much the ionospheric protons contribute to the ring current and plasmashet depends on
 556 the simulation (with or with plasmasphere), but in either case their contribution cannot be
 557 ignored. These results are consistent with the past work of *Huddleston et al.* [2005] who
 558 combined estimates of the polar wind proton fluxes with particle tracing in empirical mag-
 559 netic fields. They demonstrated that initially cold outflow can get energized in the magne-
 560 totail and be a major contributor to the plasmashet and ring current. Indeed, we similarly
 561 have cold outflow that gets energized in the magnetosphere to build the plasmashet and
 562 ring current.

568 It is particularly important to note that ionospheric protons supply cold protons to
 569 the magnetosphere that do not remain cold. It is commonly assumed that ionospheric pro-
 570 tons do not make up a significant portion of the plasmashet or ring current because they
 571 are simply at too low an energy. However, O^+ that comes out at similarly cold tempera-
 572 tures, is observed to be accelerated to tens of keV in the ring current and is also observed
 573 to be heated in other parts of the magnetosphere. There is no reason that ionospheric H^+
 574 cannot be similarly accelerated. Moreover, the polar wind is constantly supplying protons
 575 directly to the magnetosphere, unlike the solar wind protons that have to enter through re-
 576 connection or other magnetopause interactions. It should therefore be the expectation,
 577 rather than the exception, that ionospheric protons are significant contributors to warm and
 578 hot populations in the magnetosphere.

579 As an illustration of this last point, in Figure 11 we demonstrate the heating that an
 580 initially cold ionospheric H^+ particle can undergo in the magnetosphere. In this figure, we

581 follow “particles” moving along with the ionospheric H^+ fluid velocity near 5UT launched
582 from a location above the dayside MHD inner boundary. These are not true particles as
583 they follow the bulk fluid velocity, but can be rather thought of as corks dropped in the
584 river and picked up by the current. The surface of each particle is painted with a color in-
585 dicating the ionospheric H^+ temperature thus illustrating how the temperature changes as
586 parcel of plasma travels through the magnetosphere. We find that ionospheric H^+ at the
587 start of the trace near the inner boundary is around 10 eV. As you follow the path of par-
588 ticles out into the lobes to the magnetotail, the temperature grows to nearly 100 eV. When
589 the ionospheric H^+ hits the tail and starts to convect inward due to the cross tail electric
590 field the temperature rapidly increases to 1-2 keV and then to 4-7 keV. Note that the tran-
591 sition from 100eV to 1-2keV is very fast once the plasma feels the cross tail electric field,
592 and happens within a few Earth radii. The now heated ionospheric H^+ contributes to the
593 formation of the plasmasheet and warm plasma cloak [Chappell *et al.*, 2008]. Only one
594 trajectory is analyzed here to illustrate the point, but other trajectories tell a similar story.
595 These results corroborate the picture put forward by Huddleston *et al.* [2005] who followed
596 similar trajectories illustrating how cold ionospheric H^+ is heated.

597 In our simulations we also found significant hemispheric asymmetry of outflow with
598 important consequences for magnetospheric composition. In particular, we found that the
599 outflow was stronger in the northern summer hemisphere and weaker in the southern win-
600 ter hemisphere. We also found that the O^+ exhibited a much stronger seasonal variation
601 than H^+ . This result is qualitatively consistent with the observed seasonal asymmetry in
602 a study using Polar data [Lennartsson *et al.*, 2004]. Asymmetric outflow is further found
603 to fill the magnetospheric lobes asymmetrically with the northern lobe receiving more
604 ionospheric plasma with a higher proportion of O^+ and the southern lobe receiving less
605 ionospheric plasma with a higher proportion of H^+ . Although not studied here, we expect
606 this asymmetric lobe filling to have consequences for reconnection in the tail. For exam-
607 ple, asymmetries in outflow are suggested to result in flapping of the magnetotail [Barakat
608 *et al.*, 2015]. Beyond this, we speculate that asymmetric lobe filling can be expected to
609 create asymmetric O^+ density conditions near the nightside reconnection site. Recent work
610 by Kolstøet *et al.* [2020] using PIC simulations indicate that such conditions can cause asym-
611 metries in the diffusion region and motion of the reconnection site.

612 The final focus of our simulation was on the potential consequences of the plasma-
613 sphere on the broader geospace system. We found that when the plasmasphere encounters
614 the dayside magnetopause, the global reconnection rate decreases as indicated by the cross
615 polar cap potential. This is consistent with expectations from prior studies [Borovsky and
616 Steinberg, 2006; Ouellette *et al.*, 2016; Walsh *et al.*, 2014]. Beyond these past studies, we
617 were able to demonstrate a system-wide impact as the diminished reconnection rate re-
618 duced the effectiveness of the solar wind - magnetosphere coupling. This resulted in re-
619 duced outflow leaving the ionosphere, a different composition of outflow leaving the iono-
620 sphere, changes in the plasma sheet composition, and changes in the ring current intensity
621 and composition. These changes are found to begin shortly after the plume’s arrival at the
622 magnetopause where it raises the density near the reconnection separator and, interest-
623 ingly, causes the separator to twist locally. The timing of these system level impacts is an
624 interesting topic worthy of future investigation. For now, we only note that the earliest ef-
625 fect in the reduction of the O^+ fluence occurs about 30 minutes after the plume arrival at
626 the magnetopause and becomes sustained after about 2.5 hours. It is important to note that
627 the plasmasphere, which is extremely cold and by itself carries very little energy density,
628 can cause broad changes to the magnetosphere including the relative supply of plasma and
629 the intensity of the warm and hot constituents. This result implies that the preconditioning
630 of the plasmasphere may be important for storm strength and progression. To our knowl-
631 edge, this is the first time such a far reaching system-wide impact of the plasmasphere has
632 been demonstrated in either data or simulations.

In conclusion, our simulations indicate that the ionosphere cannot be neglected as a source of plasma when trying to understand geomagnetic storms. This is true for high latitude outflow as well as low latitude outflow that forms the plasmasphere. Additionally, it is improper to assume that all protons in the magnetosphere come from the solar wind. Our study, however, is only for one fairly modest geomagnetic event and future work is required to understand how well these conclusions hold for storms of different intensity and with different solar ionizing flux.

Acknowledgments

A. Glocer and M.-C. Fok acknowledge support from NASA Heliophysics Internal Scientist Funding Model (HISFM18-0006), and the Heliophysics Grand Challenge Research program (16-HGCR16_2-0008). We acknowledge valuable support from and discussion with The Center for the Unified Study of Interhemispheric Asymmetries (CUSIA). We further acknowledge valuable discussion organized by the International Space Science Institute (ISSI), in particular with the team studying cold plasma of ionospheric origin. Resources supporting this work were provided by the NASA High-End Computing (HEC) Program through the NASA Advanced Supercomputing (NAS) Division at Ames Research Center. All modeling tools described in publication are available online through the University of Michigan for download with the SWMF. The model output data used in production of all figures has been made available online for download at <http://doi.org/10.5281/zenodo.3767201>. We acknowledge the HOPE instrument team for making all RBSP-ECT data publicly available at the Web site <http://www.RBSP-ect.lanl.gov/>. We also acknowledge the ACE SWEPAM and MAG teams for making the solar wind data available through the Goddard Space Flight Center Space Physics Data Facility (<https://spdf.gsfc.nasa.gov/>). We would also like to acknowledge the SpacePy project which was used in the production of some of the figures. The authors would also like to thank S. Solomon for making the GLOW model available.

References

- Andre, M., and C. M. Cully (2012), Low-energy ions: A previously hidden solar system particle population, *Geophysical Research Letters*, *39*(3), doi:10.1029/2011GL050242.
- Axford, W. I. (1968), The polar wind and the terrestrial helium budget, *J. Geophys. Res.*, *73*, 68,55.
- Barakat, A. R., and R. W. Schunk (2001), Effects of wave-particle interactions on the dynamic behavior of the generalized polar wind, *Journal of Atmospheric and Solar-Terrestrial Physics*, *63*, 75–83, doi:10.1016/S1364-6826(00)00106-1.
- Barakat, A. R., J. V. Eccles, and R. W. Schunk (2015), Effects of geographic-geomagnetic pole offset on ionospheric outflow: Can the ionosphere wag the magnetospheric tail?, *Geophysical Research Letters*, *42*(20), 8288–8293, doi:10.1002/2015GL065736.
- Borovsky, J. E., and J. T. Steinberg (2006), The calm before the storm in cir/magnetosphere interactions: Occurrence statistics, solar wind statistics, and magnetospheric preconditioning, *J. Geophys. Res.*, *111*, A07S10.
- Brinton, H. C., J. M. Grebowsky, and H. G. Mayr (1971), Altitude Variation of Ion Composition in the Midlatitude Trough Region: Evidence for Upward Plasma Flow, *J. Geophys. Res.*, *76*, 3738–3745, doi:10.1029/JA076i016p03738.
- Chappell, C. R., T. E. Moore, and J. H. Waite (1987), The ionosphere as a fully adequate source of plasma for the earth's magnetosphere, *J. Geophys. Res.*, *92*, 5896–5910.
- Chappell, C. R., M. M. Huddleston, T. E. Moore, B. L. Giles, and D. C. Delcourt (2008), Observations of the warm plasma cloak and an explanation of its formation in the magnetosphere, *Journal of Geophysical Research: Space Physics*, *113*(A9), doi:10.1029/2007JA012945.
- De Zeeuw, D., S. Sazykin, R. Wolf, T. Gombosi, A. Ridley, and G. Tóth (2004), Coupling of a global MHD code and an inner magnetosphere model: Initial results, *J. Geophys.*

- 684 *Res.*, 109(A12), A12,219, doi:10.1029/2003JA010,366.
- 685 Engwall, E., A. I. Eriksson, C. M. Cully, M. André, R. Torbert, and H. Vaith (2009),
 686 Earth's ionospheric outflow dominated by hidden cold plasma, *Nature Geoscience*,
 687 2(1), 24–27.
- 688 Fok, M., R. A. Wolf, R. W. Spiro, and T. E. Moore (2001), Comprehensive com-
 689 putational model of Earth's ring current, *J. Geophys. Res.*, 106, 8417–8424, doi:
 690 10.1029/2000JA000235.
- 691 Fok, M.-C., Y. Ebihara, T. E. Moore, D. M. Ober, and K. A. Keller (2005), *Geospace*
 692 *Storm Processes Coupling the Ring Current, Radiation Belt and Plasmasphere*, pp. 207–
 693 220, American Geophysical Union (AGU), doi:10.1029/159GM16.
- 694 Fok, M.-C., A. Glocer, Q. Zheng, R. B. Horne, N. P. Meredith, J. M. Albert, and T. Nagai
 695 (2011), Recent developments in the radiation belt environment model, *Journal of Atmo-*
 696 *spheric and Solar-Terrestrial Physics*, 73, 1435–1443, doi:10.1016/j.jastp.2010.09.033.
- 697 Fok, M.-C., N. Y. Buzulukova, S.-H. Chen, A. Glocer, T. Nagai, P. Valek, and J. D. Perez
 698 (2014), The comprehensive inner magnetosphere-ionosphere model, *Journal of Geo-*
 699 *physical Research: Space Physics*, 119(9), 7522–7540, doi:10.1002/2014JA020239,
 700 2014JA020239.
- 701 Glocer, A., T. I. Gombosi, G. Toth, K. C. Hansen, A. J. Ridley, and A. Nagy (2007), Polar
 702 wind outflow model: Saturn results, *J. Geophys. Res.*, 112, doi:10.1029/2006JA011755.
- 703 Glocer, A., G. Toth, T. Gombosi, and D. Welling (2009), Modeling ionospheric outflows
 704 and their impact on the magnetosphere, initial results, *J. Geophys. Res.*, 114(A05216),
 705 doi:10.1029/2009JA014053.
- 706 Glocer, A., G. Tóth, Y. Ma, T. Gombosi, J.-C. Zhang, and L. M. Kistler (2009), Multifluid
 707 Block-Adaptive-Tree Solar wind Roe-type Upwind Scheme: Magnetospheric composi-
 708 tion and dynamics during geomagnetic storms - Initial results, *Journal of Geophysical*
 709 *Research (Space Physics)*, 114(A13), A12203, doi:10.1029/2009JA014418.
- 710 Glocer, A., N. Kitamura, G. Toth, and T. Gombosi (2012), Modeling solar zenith angle
 711 effects on the polar wind, *Journal of Geophysical Research: Space Physics*, 117(A4),
 712 n/a–n/a, doi:10.1029/2011JA017136, a04318.
- 713 Glocer, A., M. Fok, X. Meng, G. Toth, N. Buzulukova, S. Chen, and K. Lin (2013),
 714 CRCM + BATS-R-US two-way coupling, *Journal of Geophysical Research (Space*
 715 *Physics)*, 118, 1635–1650, doi:10.1002/jgra.50221.
- 716 Glocer, A., J. Dorelli, G. Toth, C. M. Komar, and P. A. Cassak (2016), Separator recon-
 717 nection at the magnetopause for predominantly northward and southward imf: Tech-
 718 niques and results, *Journal of Geophysical Research: Space Physics*, 121(1), 140–156,
 719 doi:10.1002/2015JA021417.
- 720 Glocer, A., G. Khazanov, and M. Liemohn (2017), Photoelectrons in the quiet po-
 721 lar wind, *Journal of Geophysical Research: Space Physics*, 122(6), 6708–6726, doi:
 722 10.1002/2017JA024177, 2017JA024177.
- 723 Glocer, A., G. Toth, and M.-C. Fok (2018), Including kinetic ion effects in the coupled
 724 global ionospheric outflow solution, *Journal of Geophysical Research: Space Physics*,
 725 123(4), 2851–2871, doi:10.1002/2018JA025241.
- 726 Gloeckler, G., and D. C. Hamilton (1987), AMPTE ion composition results, *Physica*
 727 *Scripta*, T18, 73–84, doi:10.1088/0031-8949/1987/t18/009.
- 728 Hoffman, J. H. (1970), Studies of the composition of the ionosphere with a magnetic de-
 729 flection mass spectrometer, *Int. J. Mass Spectrom. Ion Phys.*, 4(315).
- 730 Hoffman, J. H., and W. H. Dodson (1980), Light ion concentrations and fluxes in the
 731 polar regions during magnetically quiet times, *J. Geophys. Res.*, 85, 626–632, doi:
 732 10.1029/JA085iA02p00626.
- 733 Hoffman, J. H., W. H. Dodson, C. R. Lippincott, and H. D. Hammack (1974), Initial
 734 ion composition results from the Isis 2 satellite, *J. Geophys. Res.*, 79, 4246–4251, doi:
 735 10.1029/JA079i028p04246.
- 736 Huddleston, M. M., C. R. Chappell, D. C. Delcourt, T. E. Moore, B. L. Giles, and M. O.
 737 Chandler (2005), An examination of the process and magnitude of ionospheric plasma

- supply to the magnetosphere, *J. Geophys. Res.*, *110*, 12,202, doi:10.1029/2004JA010401.
- Keller, K. A., M. Fok, A. Narock, M. Hesse, L. Rastaetter, M. M. Kuznetsova, T. I. Gombosi, and D. L. DeZeeuw (2005), Effect of multiple substorms on the buildup of the ring current, *J. Geophys. Res.*, *110*, A08,202, doi:10.1029/2004JA010,747.
- Kolstø, H. M., M. Hesse, C. Norgren, P. Tenfjord, S. F. Spinnangr, and N. Kwagala (2020), Collisionless magnetic reconnection in an asymmetric oxygen density configuration, *Geophysical Research Letters*, *47*(1), e2019GL085,359, doi:10.1029/2019GL085359, e2019GL085359 10.1029/2019GL085359.
- Lee, J. H., and V. Angelopoulos (2014), On the presence and properties of cold ions near earth's equatorial magnetosphere, *Journal of Geophysical Research: Space Physics*, *119*(3), 1749–1770, doi:10.1002/2013JA019305.
- Lee, S. H., H. Zhang, Q.-G. Zong, A. Otto, H. Rme, and E. Liebert (2016), A statistical study of plasmaspheric plumes and ionospheric outflows observed at the dayside magnetopause, *Journal of Geophysical Research: Space Physics*, *121*(1), 492–506, doi:10.1002/2015JA021540.
- Lemaire, J., and M. Scherer (1970), Model of the polar ion-exosphere, *Planetary and Space Science*, *18*(1), 103 – 120, doi:http://dx.doi.org/10.1016/0032-0633(70)90070-X.
- Lennartsson, O. W., H. L. Collin, and W. K. Peterson (2004), Solar wind control of earth's h+ and o+ outflow rates in the 15-ev to 33-kev energy range, *Journal of Geophysical Research: Space Physics*, *109*(A12), doi:10.1029/2004JA010690.
- Lennartsson, W., R. D. Sharp, E. G. Shelley, R. G. Johnson, and H. Balsiger (1981), Ion composition and energy distribution during 10 magnetic storms, *J. Geophys. Res.*, *86*, 4628–4638, doi:10.1029/JA086iA06p04628.
- Meng, X., G. Tth, M. W. Liemohn, T. I. Gombosi, and A. Runov (2012), Pressure anisotropy in global magnetospheric simulations: A magnetohydrodynamics model, *Journal of Geophysical Research (Space Physics)*, *117*, 8216, doi:10.1029/2012JA017791.
- Meng, X., G. Tth, A. Gloer, M.-C. Fok, and T. I. Gombosi (2013), Pressure anisotropy in global magnetospheric simulations: Coupling with ring current models, *Journal of Geophysical Research: Space Physics*, *118*(9), 5639–5658, doi:10.1002/jgra.50539.
- Moore, T. E., M.-C. Fok, M. O. Chandler, C. R. Chappell, S. P. Christon, D. C. Delcourt, J. Fedder, M. Huddleston, M. Liemohn, W. K. Peterson, and S. Slinker (2005), Plasma sheet and (nonstorm) ring current formation from solar and polar wind sources, *Journal of Geophysical Research: Space Physics*, *110*(A2), doi:10.1029/2004JA010563.
- Opher, M., A. Loeb, J. Drake, and G. Toth (2020), A small and round heliosphere suggested by magnetohydrodynamic modelling of pick-up ions, *Nature Astronomy*, doi:10.1038/s41550-020-1036-0.
- Ouellette, J. E., J. G. Lyon, O. J. Brambles, B. Zhang, and W. Lotko (2016), The effects of plasmaspheric plumes on dayside reconnection, *Journal of Geophysical Research: Space Physics*, *121*(5), 4111–4118, doi:10.1002/2016JA022597.
- Peromian, V., M. El-Alaoui, M. A. Abdalla, and L. M. Zelenyi (2007), A comparison of solar wind and ionospheric plasma contributions to the september 24–25, 1998 magnetic storm, *Journal of Atmospheric and Solar-Terrestrial Physics*, *69*(3), 212 – 222, doi:https://doi.org/10.1016/j.jastp.2006.07.025, global Aspects of Magnetosphere-Ionosphere Coupling.
- Peterson, W. (2002), Ionospheric influence on substorm development, in *Proceedings of the Sixth International Conference on Substorms*, University of Washington, p. 143.
- Redmon, R. J., W. K. Peterson, L. Andersson, and P. G. Richards (2012), Dawnward shift of the dayside o+ outflow distribution: The importance of field line history in o+ escape from the ionosphere, *Journal of Geophysical Research: Space Physics*, *117*(A12), doi:10.1029/2012JA018145.
- Ridley, A., T. Gombosi, and D. DeZeeuw (2004), Ionospheric control of the magnetosphere: conductance, *Annales Geophysicae*, *22*, 567–584.

- 791 Schunk, R. W., and J. J. Sojka (1997), Global ionosphere-polar wind system dur-
792 ing changing magnetic activity, *Journal of Geophysical Research*, *102*, 11,625, doi:
793 10.1029/97JA00292.
- 794 Seki, K., M. Hirahara, M. Hoshino, T. Terasawa, R. C. Elphic, Y. Saito, T. Mukai,
795 H. Hayakawa, H. Kojima, and H. Matsumoto (2003), Cold ions in the hot plasma sheet
796 of Earth's magnetotail, *Nature*, *422*(6932), 589–592, doi:10.1038/nature01502.
- 797 Shelley, E. (1986), Magnetospheric energetic ions from the earth's ionosphere, *Advances in*
798 *Space Research*, *6*(3), 121 – 132, doi:https://doi.org/10.1016/0273-1177(86)90325-X.
- 799 Shelley, E., H. I. Collin, J. K. Drake, W. Lennartsson, and A. Yau (1986), Origin of
800 plasma sheet ions: substorm and solar cycle dependence, *Eos, Transactions American*
801 *Geophysical Union*, *67*(44), 1133, doi:10.1029/EO067i044p00867.
- 802 Shelley, E. G., R. G. Johnson, and R. D. Sharp (1972), Satellite Observations of Ener-
803 getic Heavy Ions during a Geomagnetic Storm, *J. Geophys. Res.*, *77*, 6104–6110, doi:
804 10.1029/JA077i031p06104.
- 805 Solomon, S. C. (2017), Global modeling of thermospheric airglow in the far ultra-
806 violet, *Journal of Geophysical Research: Space Physics*, *122*(7), 7834–7848, doi:
807 10.1002/2017JA024314, 2017JA024314.
- 808 Solomon, S. C., P. B. Hays, and V. J. Abreu (1988), The auroral 6300 Å emission: Ob-
809 servations and modeling, *Journal of Geophysical Research: Space Physics*, *93*(A9),
810 9867–9882, doi:10.1029/JA093iA09p09867.
- 811 Strangeway, R. J., R. E. Ergun, Y.-J. Su, C. W. Carlson, and R. C. Elphic (2005), Factors
812 controlling ionospheric outflows as observed at intermediate altitudes, *Journal of Geo-*
813 *physical Research (Space Physics)*, *110*, 3221, doi:10.1029/2004JA010829.
- 814 Tóth, G., Y. J. Ma, and T. I. Gombosi (2008), Hall magnetohydrodynamics on block adap-
815 tive grids, *J. Comput. Phys.*, *227*, 6967–6984, doi:doi:10.1016/j.jcp.2008.04.010.
- 816 Tóth, G., B. van der Holst, I. V. Sokolov, D. L. de Zeeuw, T. I. Gombosi, F. Fang, W. B.
817 Manchester, X. Meng, D. Najib, K. G. Powell, Q. F. Stout, A. Glocer, Y.-J. Ma, and
818 M. Opher (2012), Adaptive numerical algorithms in space weather modeling, *Journal of*
819 *Computational Physics*, *231*, 870–903, doi:10.1016/j.jcp.2011.02.006.
- 820 Varney, R. H., M. Wiltberger, B. Zhang, W. Lotko, and J. Lyon (2016), Influence of ion
821 outflow in coupled geospace simulations: 2. sawtooth oscillations driven by physics-
822 based ion outflow, *Journal of Geophysical Research: Space Physics*, *121*(10), 9688–
823 9700, doi:10.1002/2016JA022778.
- 824 Walsh, B. M., D. G. Sibeck, Y. Nishimura, and V. Angelopoulos (2013), Statistical analy-
825 sis of the plasmaspheric plume at the magnetopause, *Journal of Geophysical Research:*
826 *Space Physics*, *118*(8), 4844–4851, doi:10.1002/jgra.50458.
- 827 Walsh, B. M., T. D. Phan, D. G. Sibeck, and V. M. Souza (2014), The plasmaspheric
828 plume and magnetopause reconnection, *Geophysical Research Letters*, *41*(2), 223–228,
829 doi:10.1002/2013GL058802.
- 830 Welling, D. T., V. K. Jordanova, S. G. Zaharia, A. Glocer, and G. Toth (2011), The effects
831 of dynamic ionospheric outflow on the ring current, *Journal of Geophysical Research*
832 *(Space Physics)*, *116*, A00J19, doi:10.1029/2010JA015642.
- 833 Wiltberger, M., W. Lotko, J. G. Lyon, P. Damiano, and V. Merkin (2010), Influence of
834 cusp o+ outflow on magnetotail dynamics in a multifluid mhd model of the magne-
835 tosphere, *Journal of Geophysical Research: Space Physics*, *115*(A10), n/a–n/a, doi:
836 10.1029/2010JA015579, a00J05.
- 837 Winglee, R. M., D. Chua, M. Brittacher, G. K. Parks, and G. Lu (2002), Global im-
838 pact of ionospheric outflows on the dynamics of the magnetosphere and cross-polar
839 cap potential, *Journal of Geophysical Research (Space Physics)*, *107*, 1237, doi:
840 10.1029/2001JA000214.
- 841 Zhang, B., O. J. Brambles, M. Wiltberger, W. Lotko, J. E. Ouellette, and J. G. Lyon
842 (2016), How does mass loading impact local versus global control on dayside recon-
843 nection?, *Geophysical Research Letters*, *43*(5), 1837–1844, doi:10.1002/2016GL068005.

844 Zhao, K., L. M. Kistler, E. J. Lund, N. Nowrouzi, N. Kitamura, and R. J. Strangeway
845 (2020), Factors controlling o+ and h+ outflow in the cusp during a geomagnetic storm:
846 Fast/teams observations, *Geophysical Research Letters*, 47(11), e2020GL086,975, doi:
847 10.1029/2020GL086975, e2020GL086975 2020GL086975.

Author Manuscript

Figure 1.

Author Manuscript

Solar Wind Drivers (GSM Coordinates)

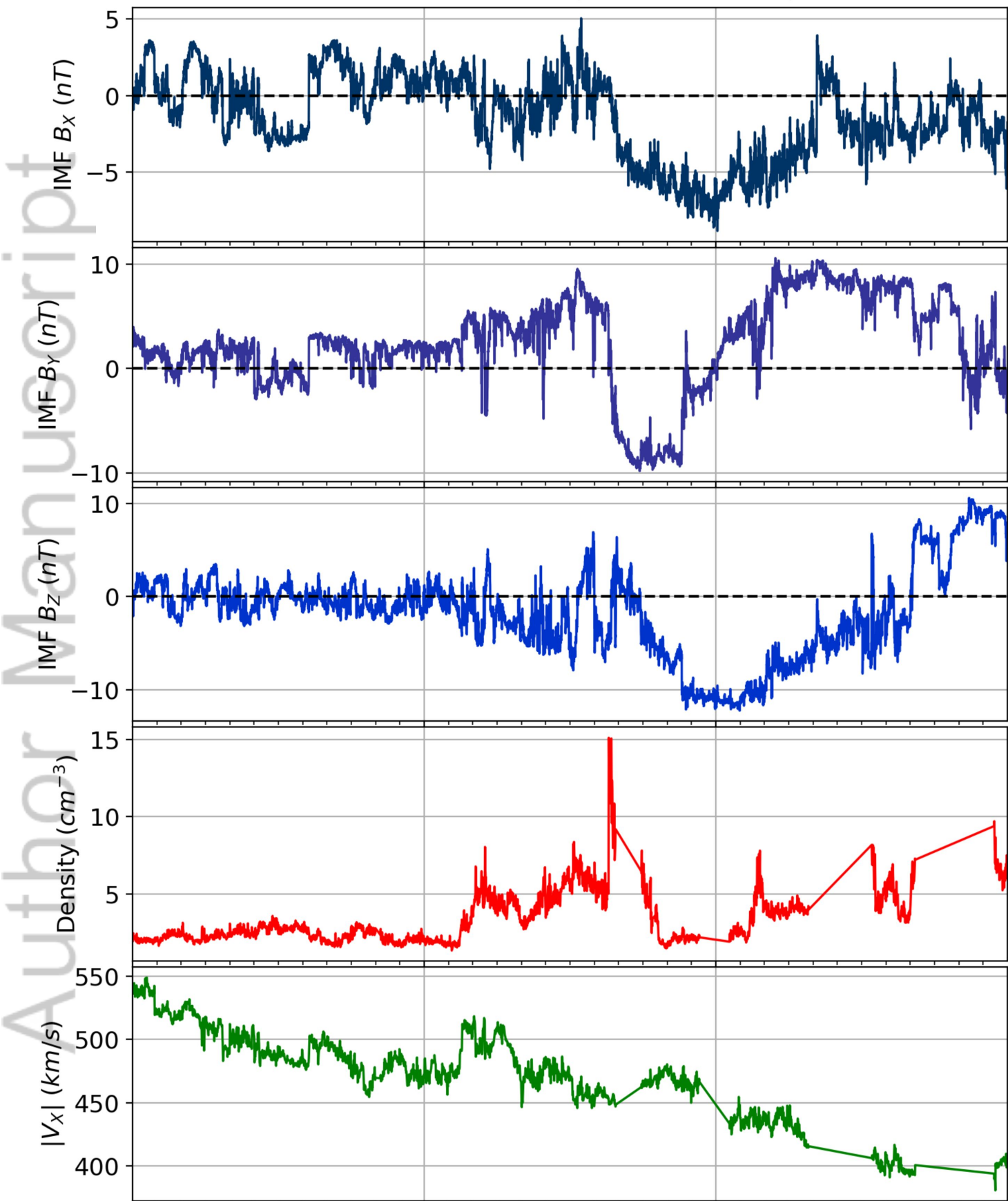


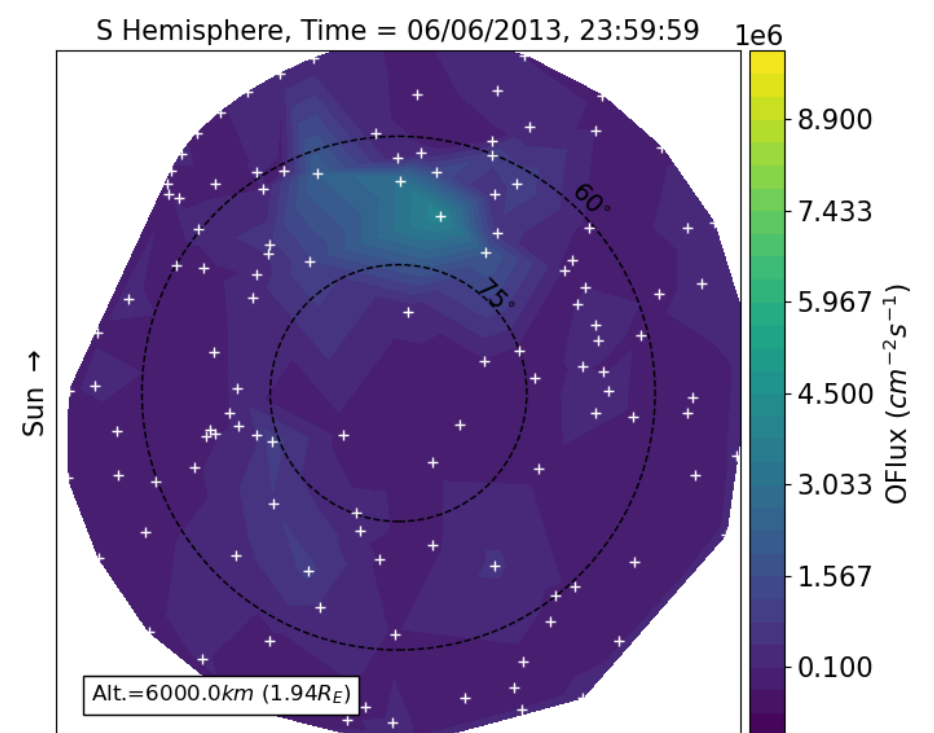
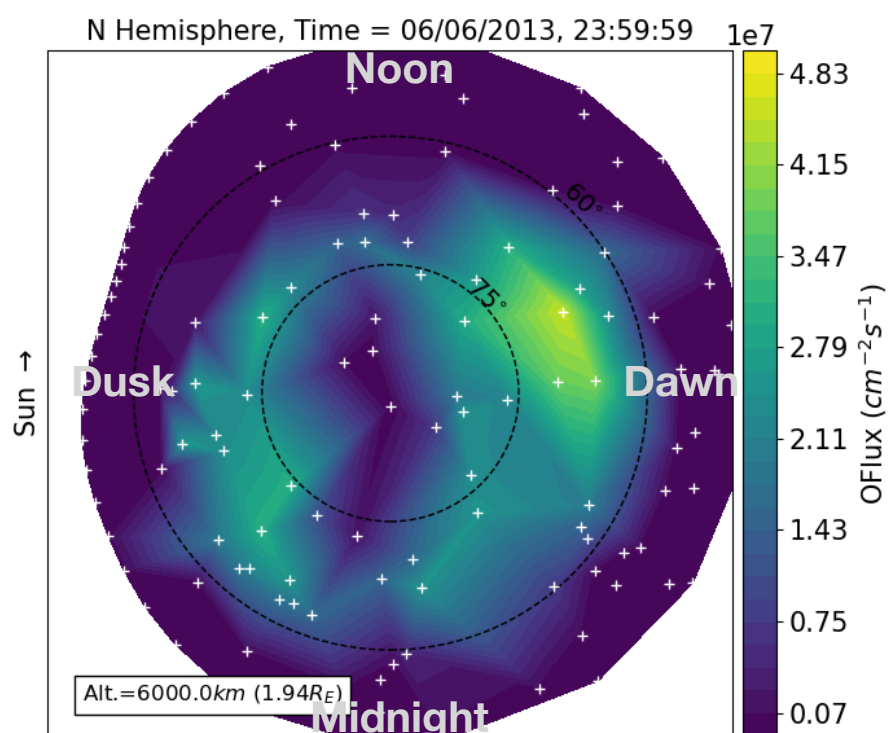
Figure 2.

Author Manuscript

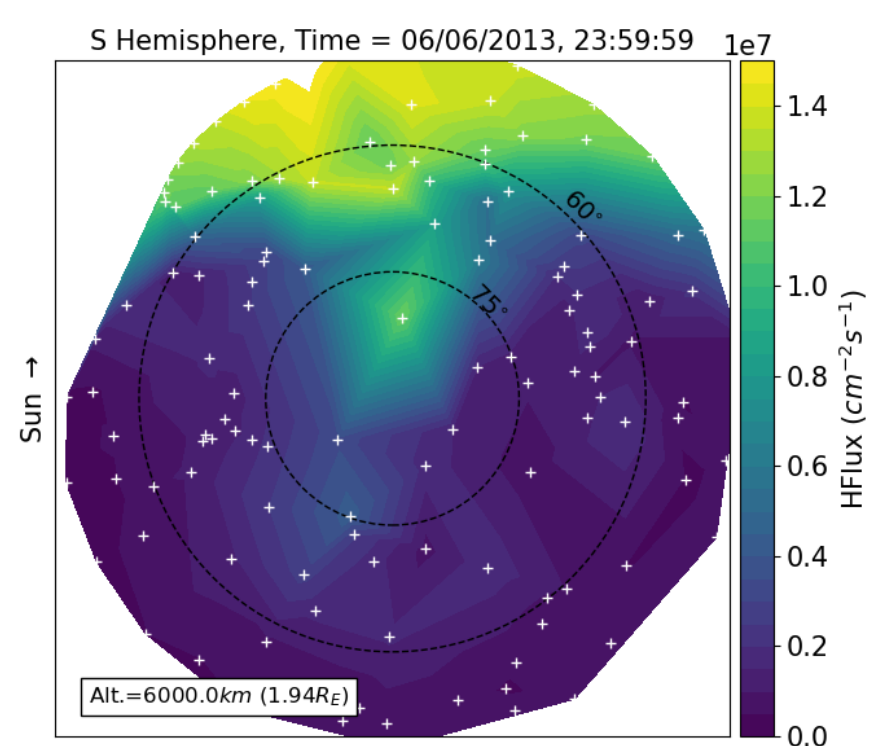
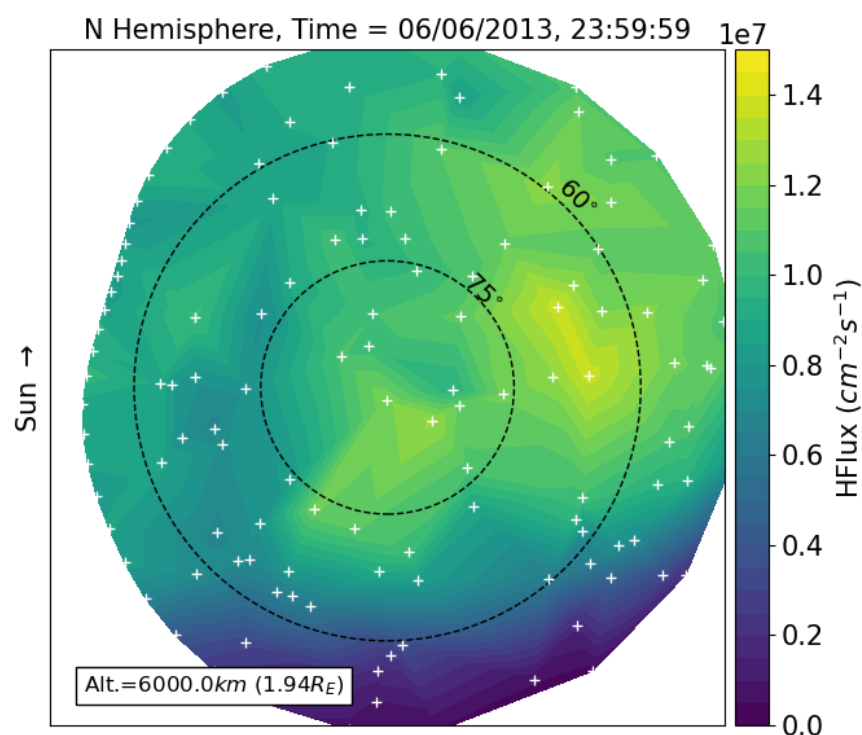
Northern Hemisphere

Southern Hemisphere

**O⁺
Flux:**

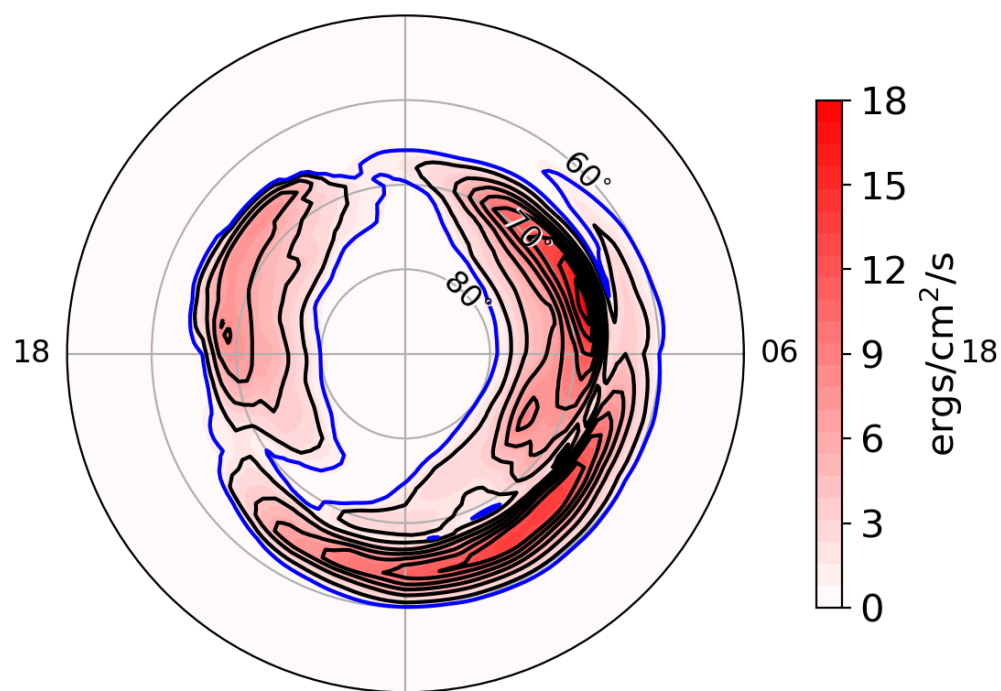


**H⁺
Flux:**



N. Precipitating Energy Flux

**e⁻
Energy
Flux:**



S. Precipitating Energy Flux

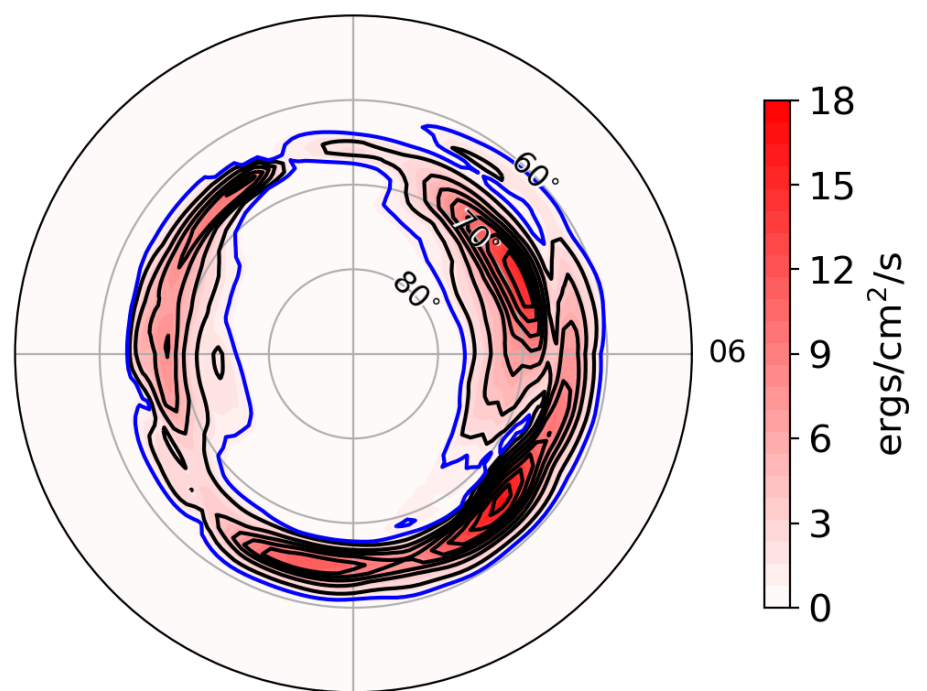


Figure 3.

Author Manuscript

Integrated Outflow Fluence

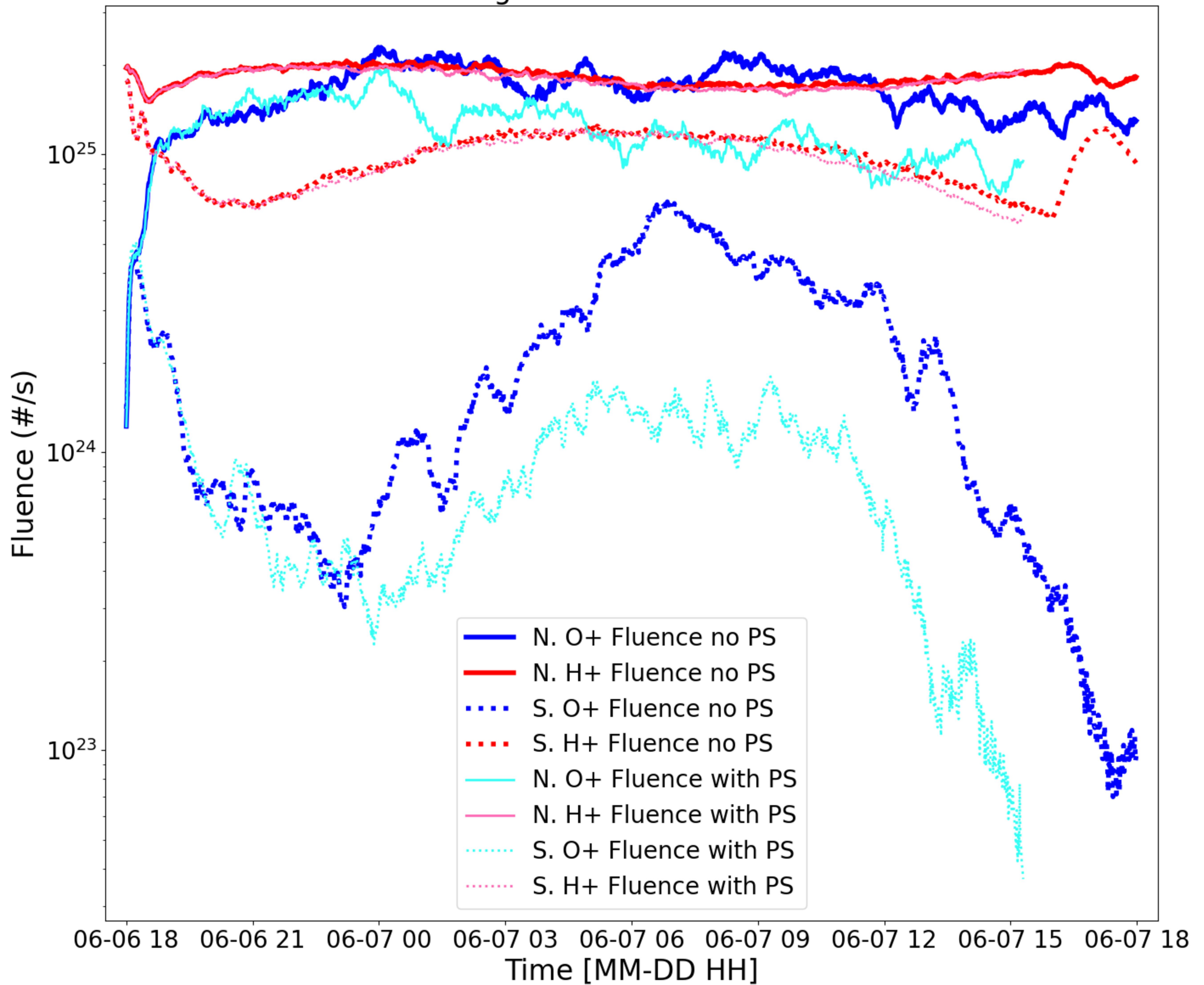


Figure 4.

Author Manuscript

Without Plasmasphere

With Plasmasphere

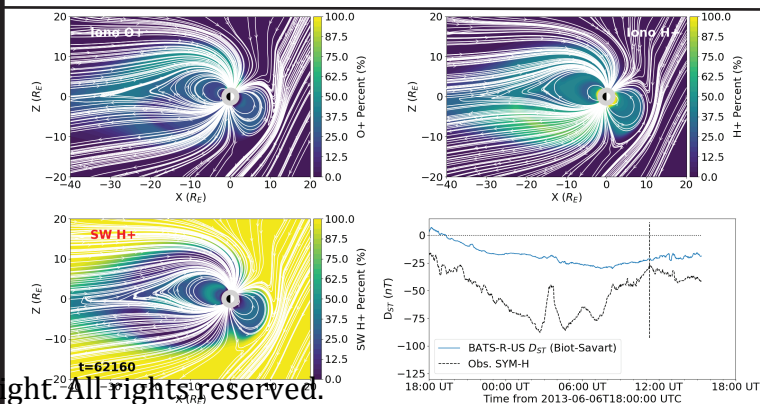
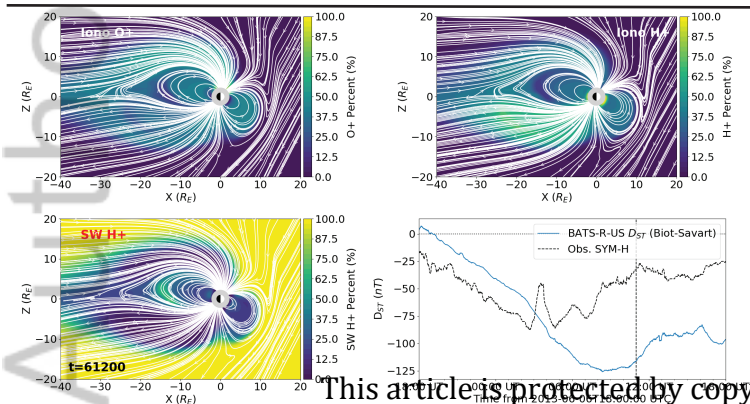
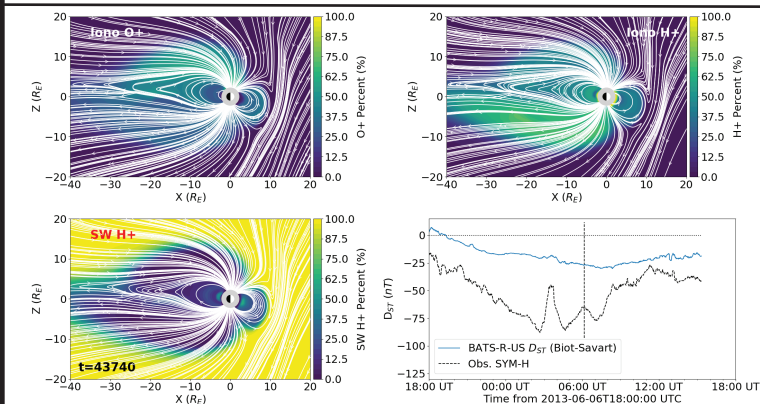
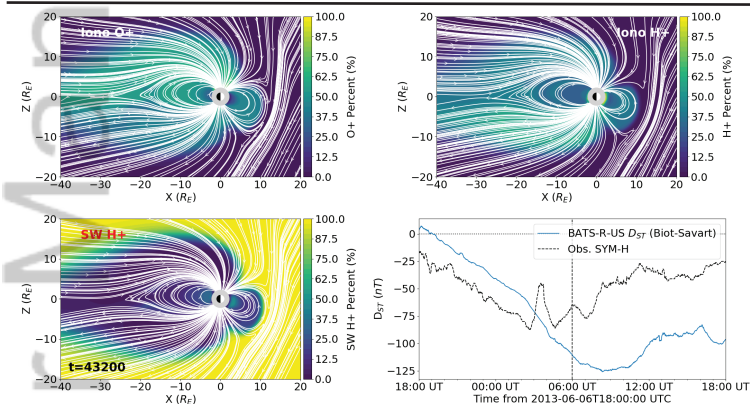
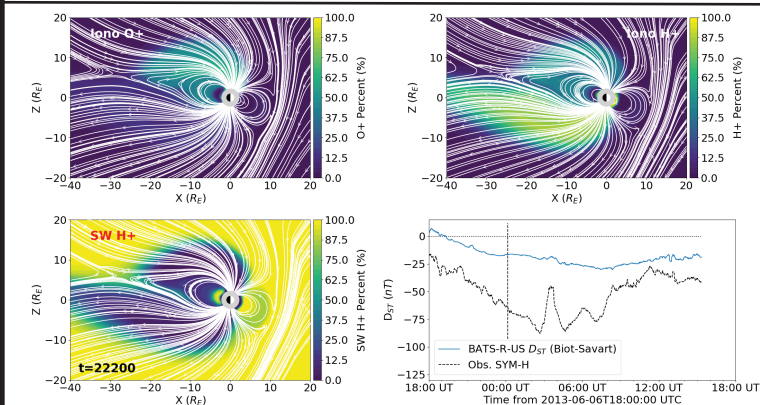
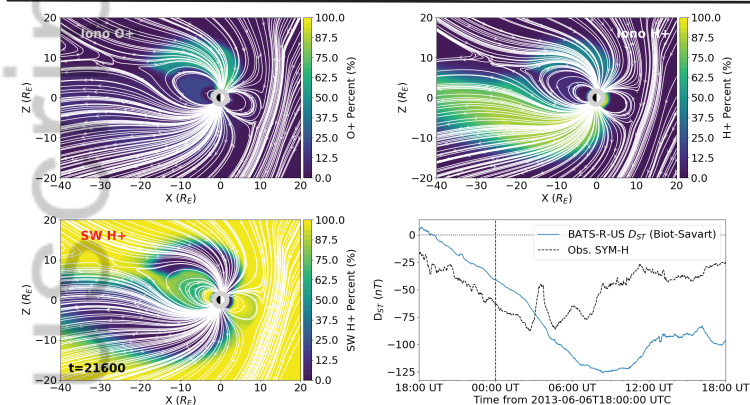
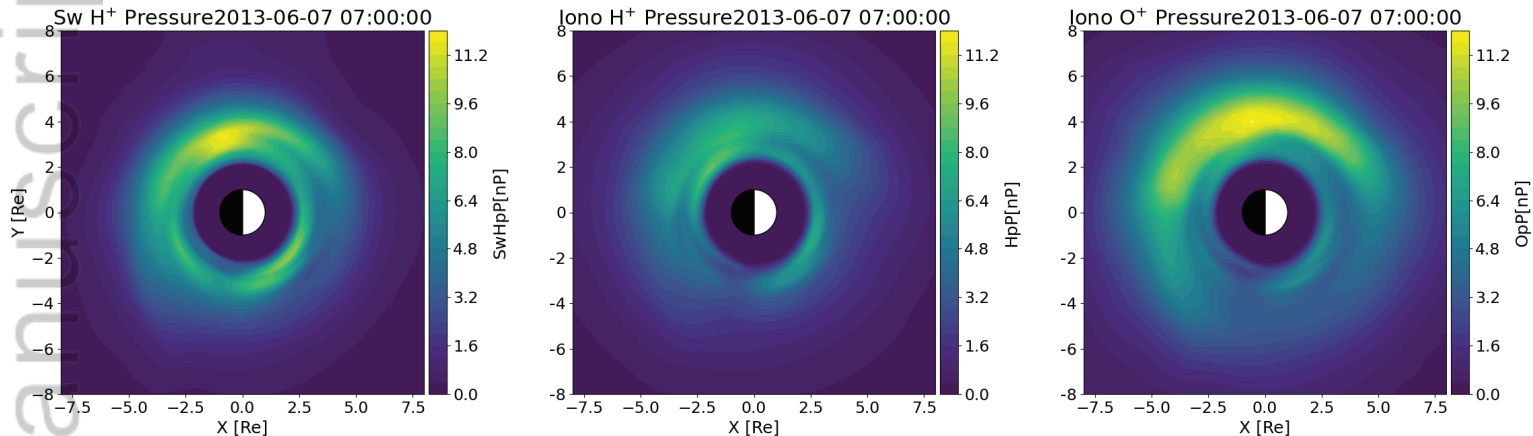


Figure 5.

Author Manuscript

Ring Current Pressure Without Plasmasphere



Ring Current Pressure With Plasmasphere

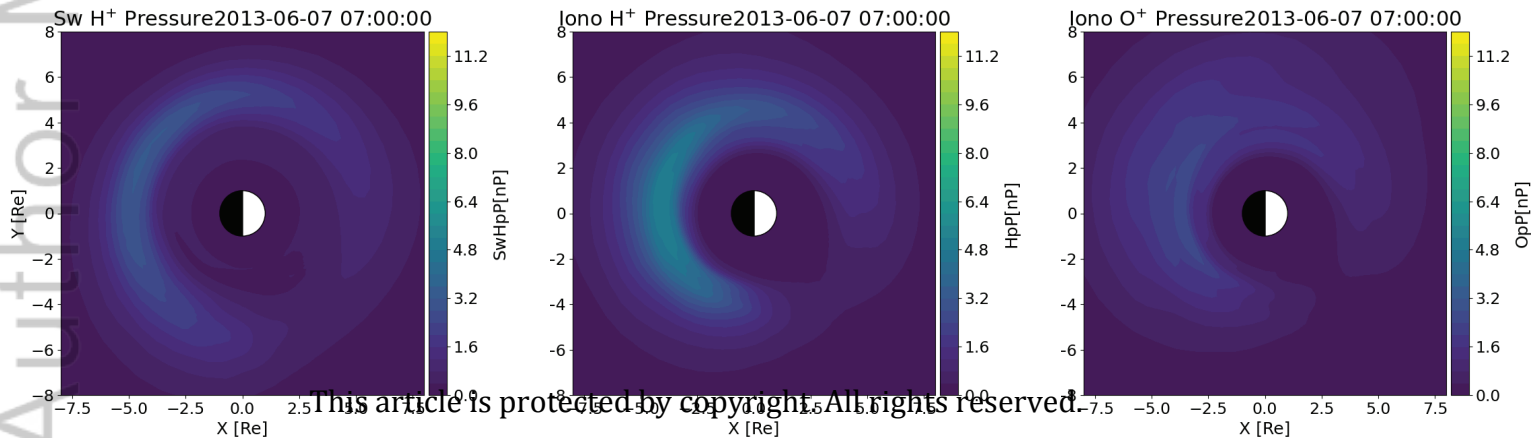
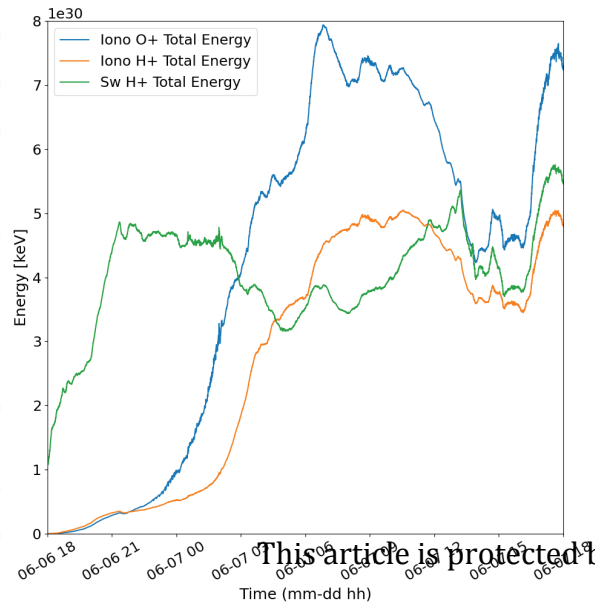


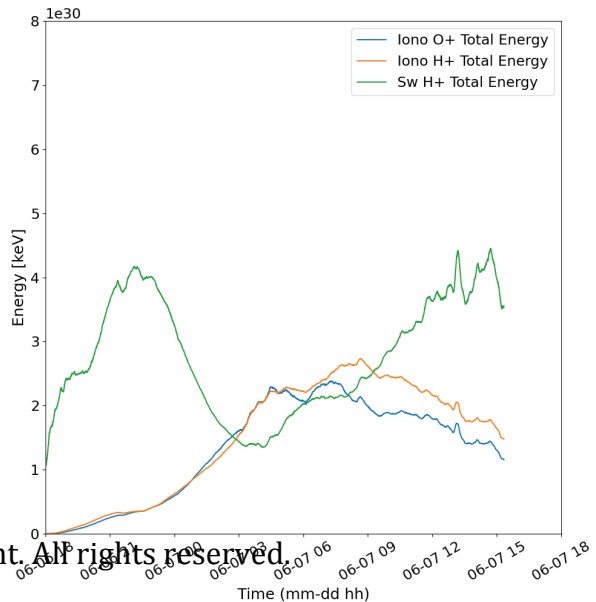
Figure 6.

Author Manuscript

Without Plasmasphere



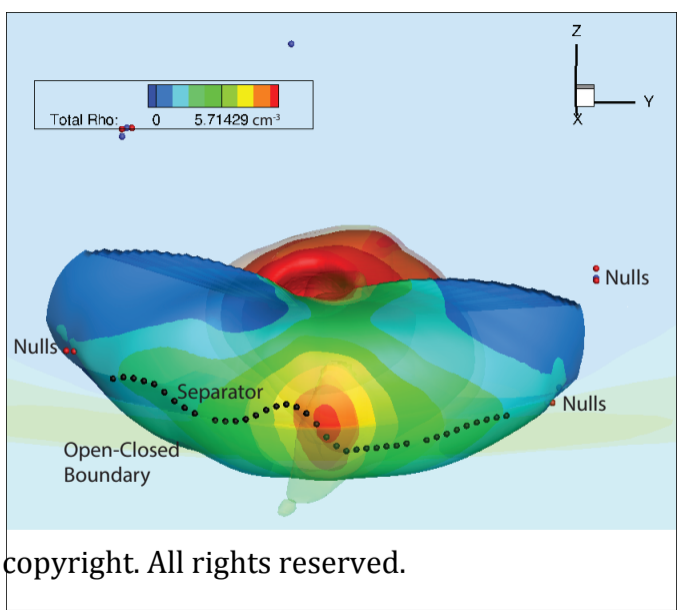
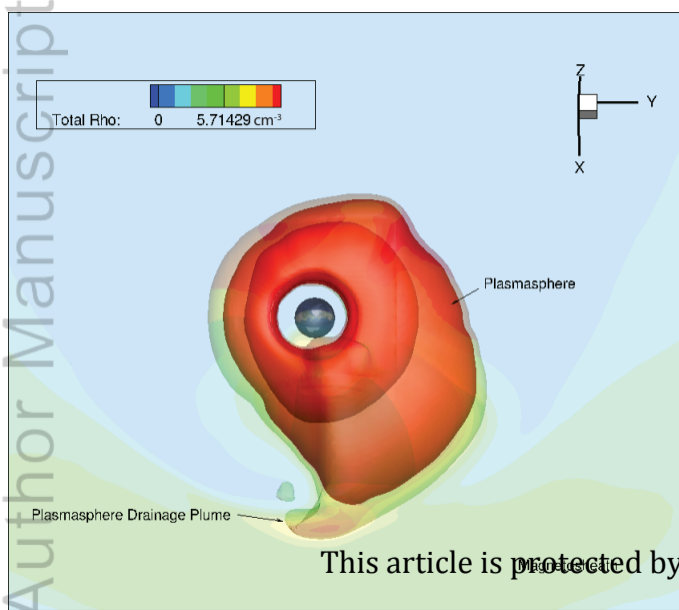
With Plasmasphere



This article is protected by copyright. All rights reserved.

Figure 7.

Author Manuscript



This article is protected by copyright. All rights reserved.

Figure 8.

Author Manuscript

CPCP With and Without Plasmasphere

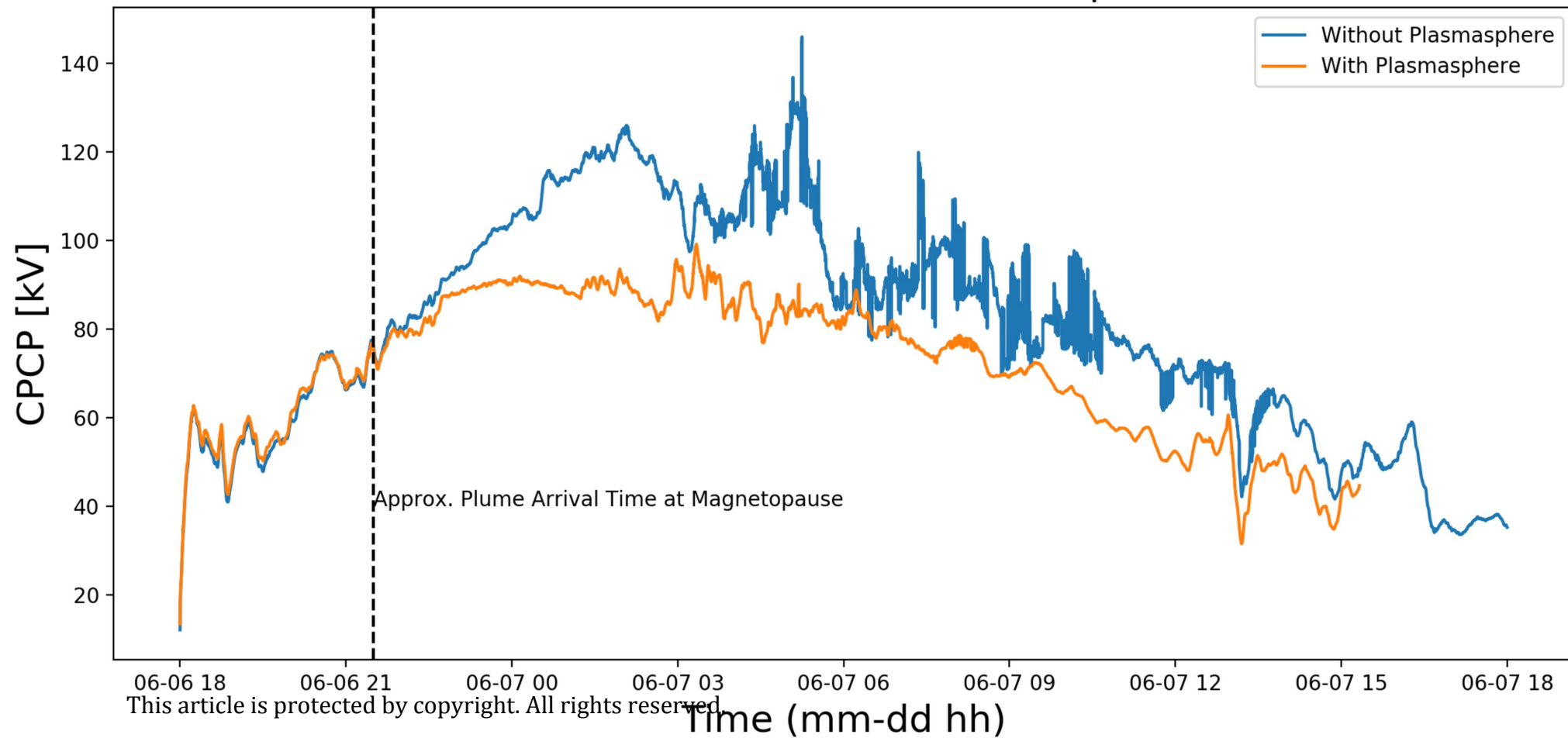
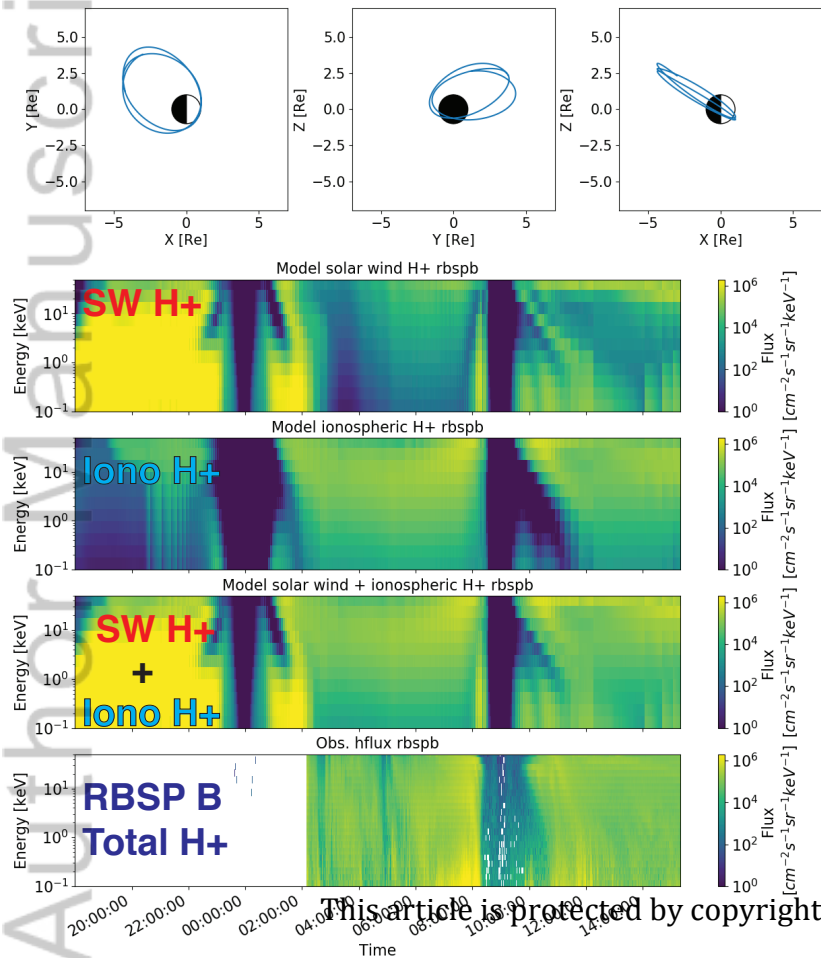


Figure 9.

Author Manuscript

With Plasmasphere



Without Plasmasphere

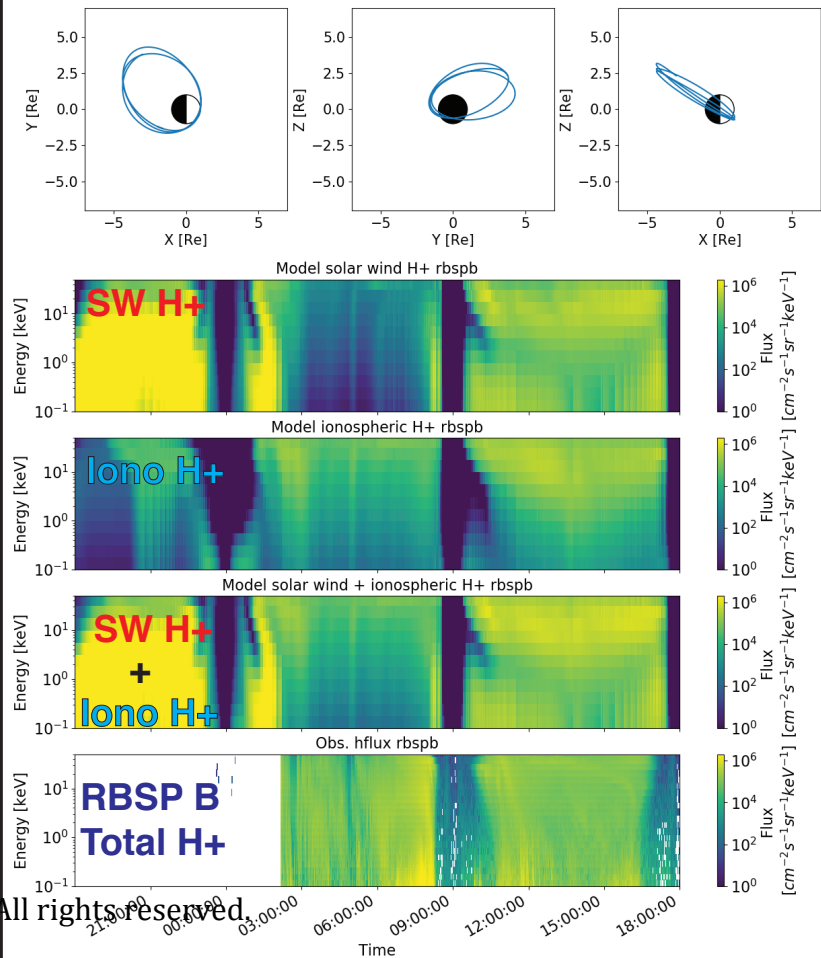
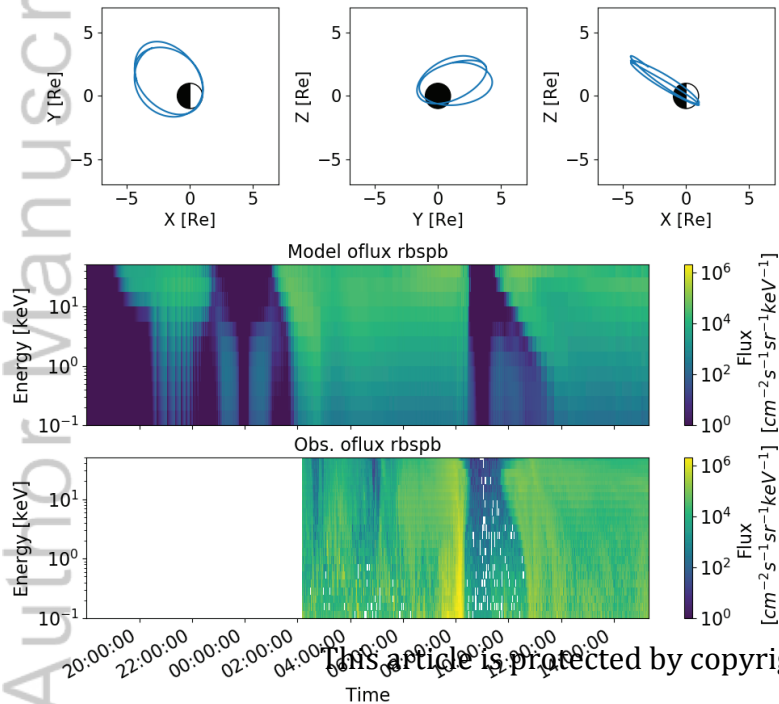


Figure 10.

Author Manuscript

With Plasmasphere



Without Plasmasphere

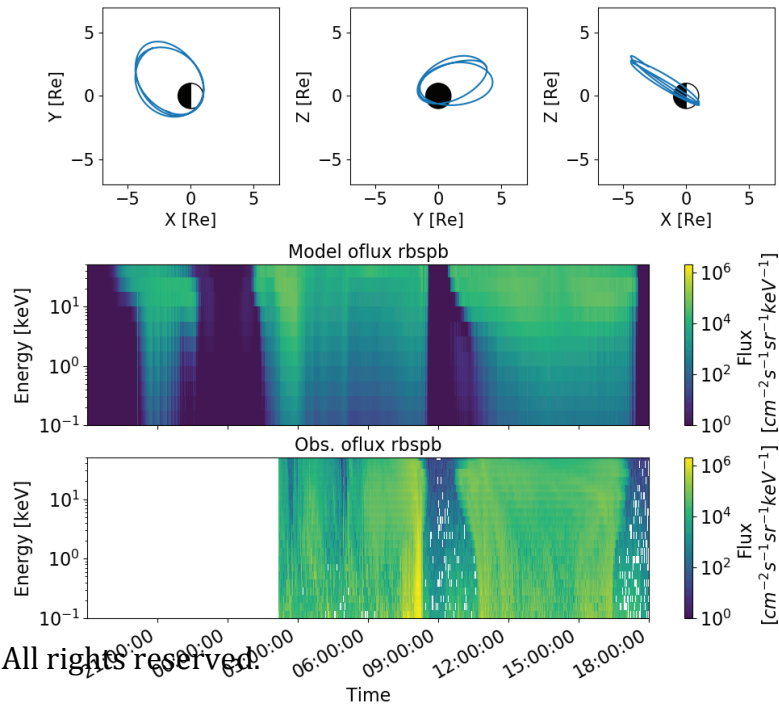
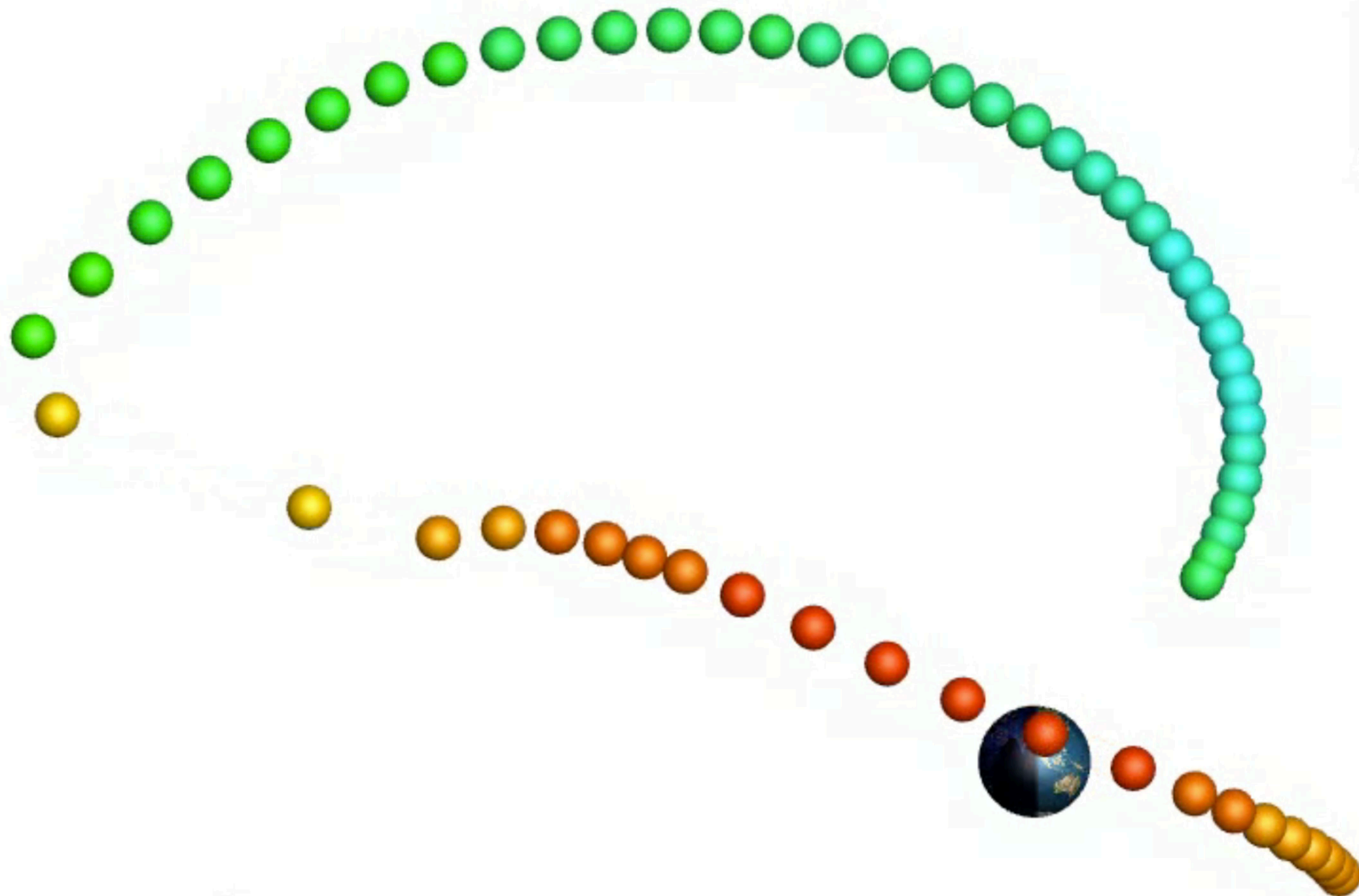
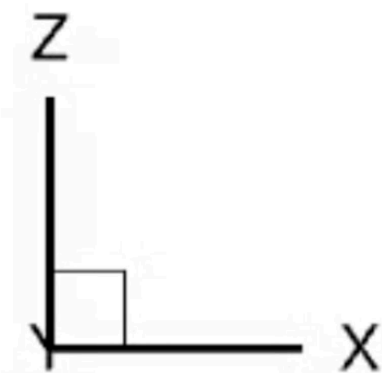
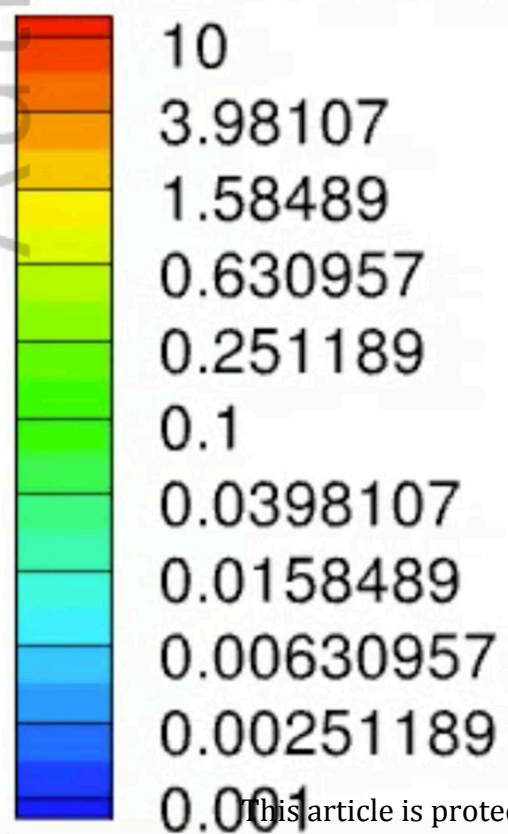


Figure 11.

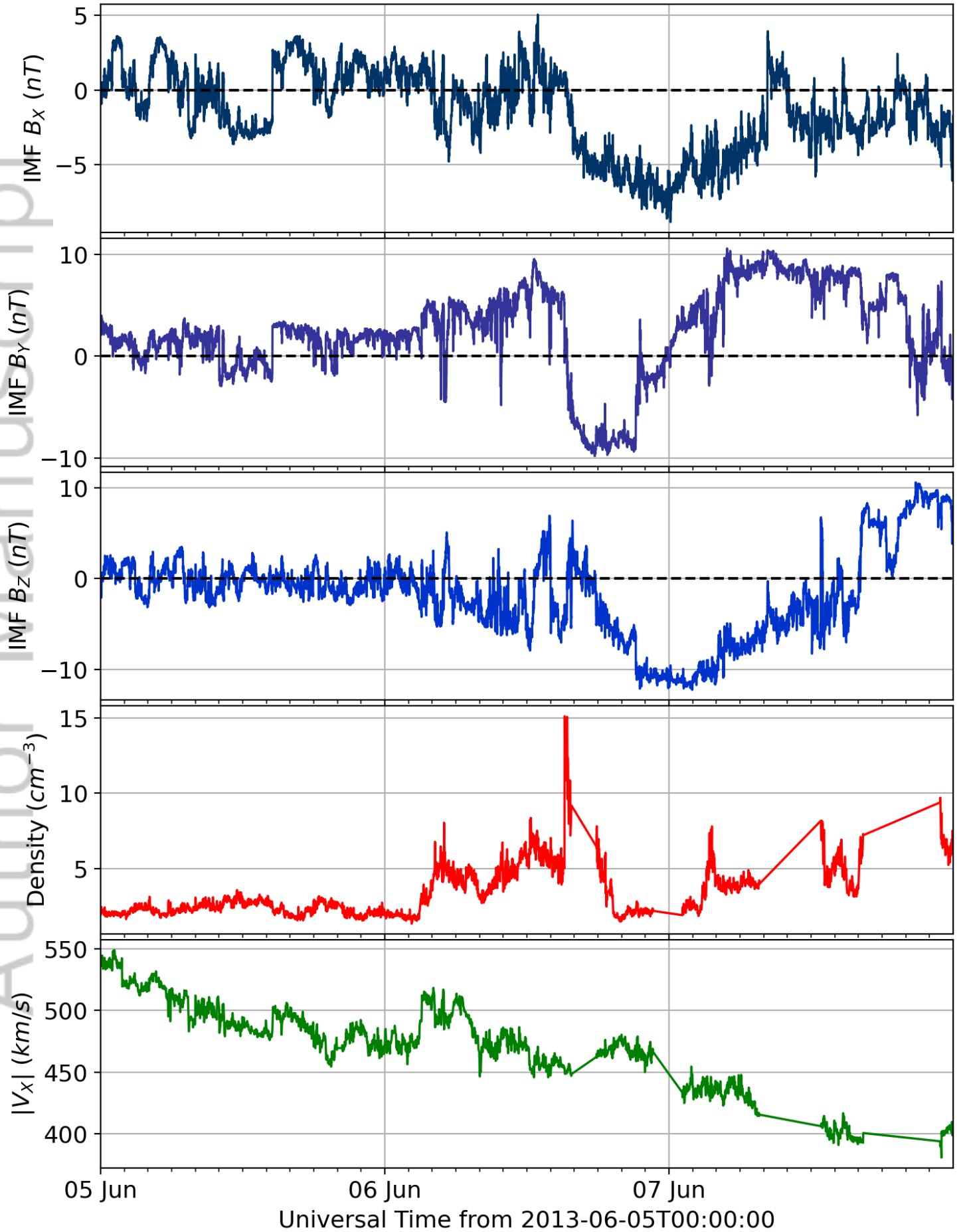
Author Manuscript



T_ionoH [keV]



Solar Wind Drivers (GSM Coordinates)

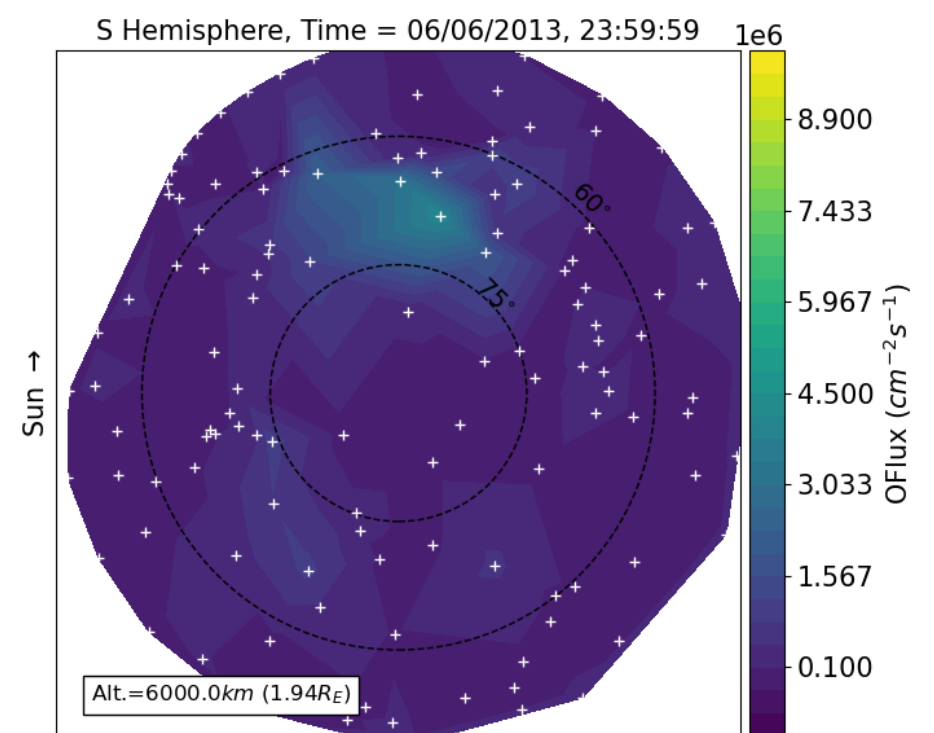
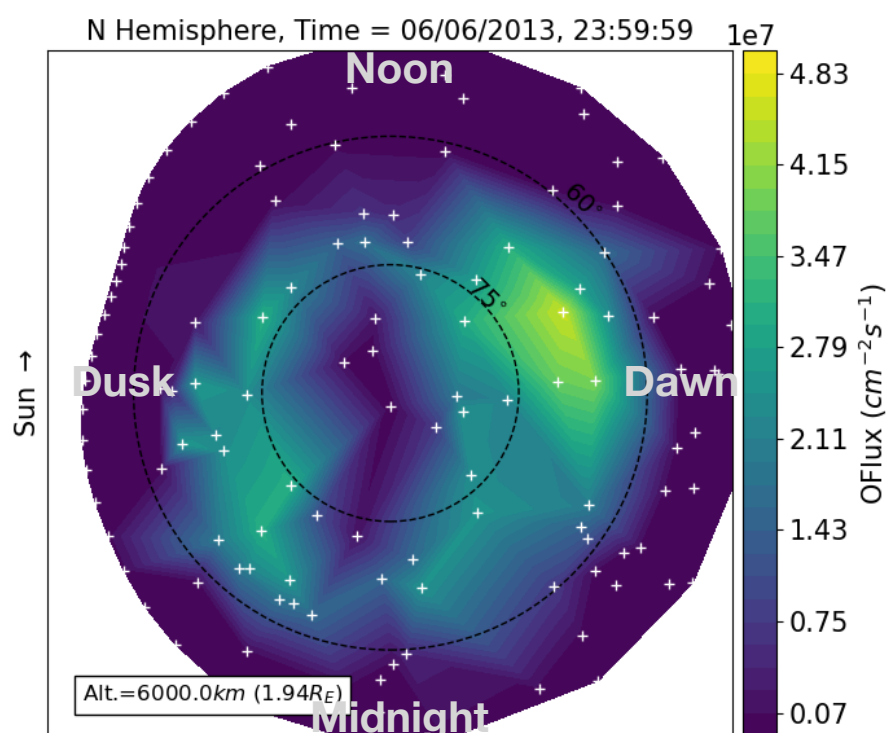


JGRA_56048_2020JA028205-f01-z-.png

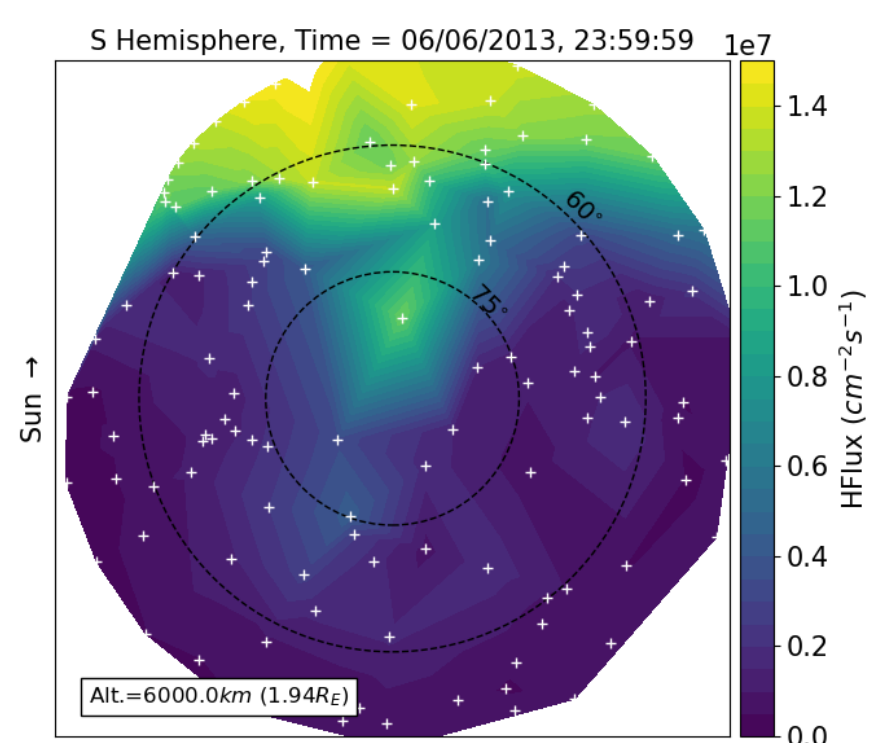
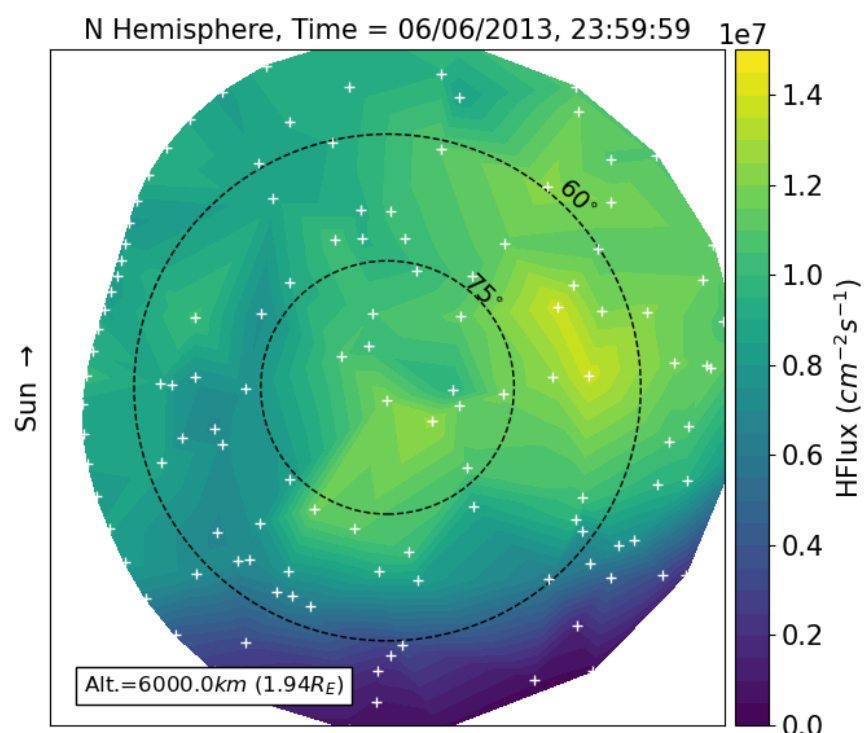
Northern Hemisphere

Southern Hemisphere

**O⁺
Flux:**

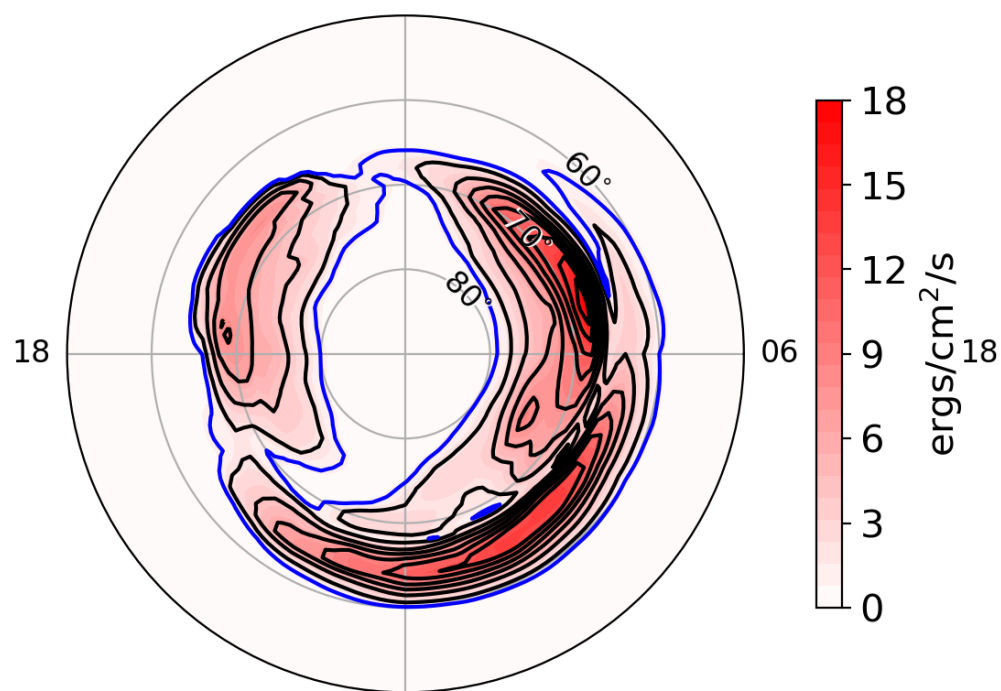


**H⁺
Flux:**

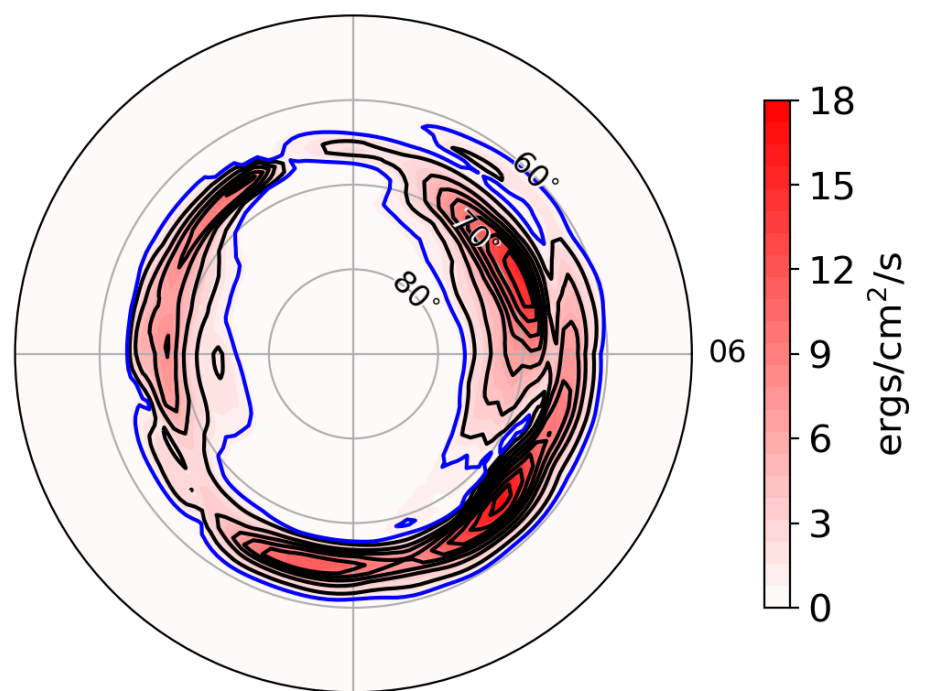


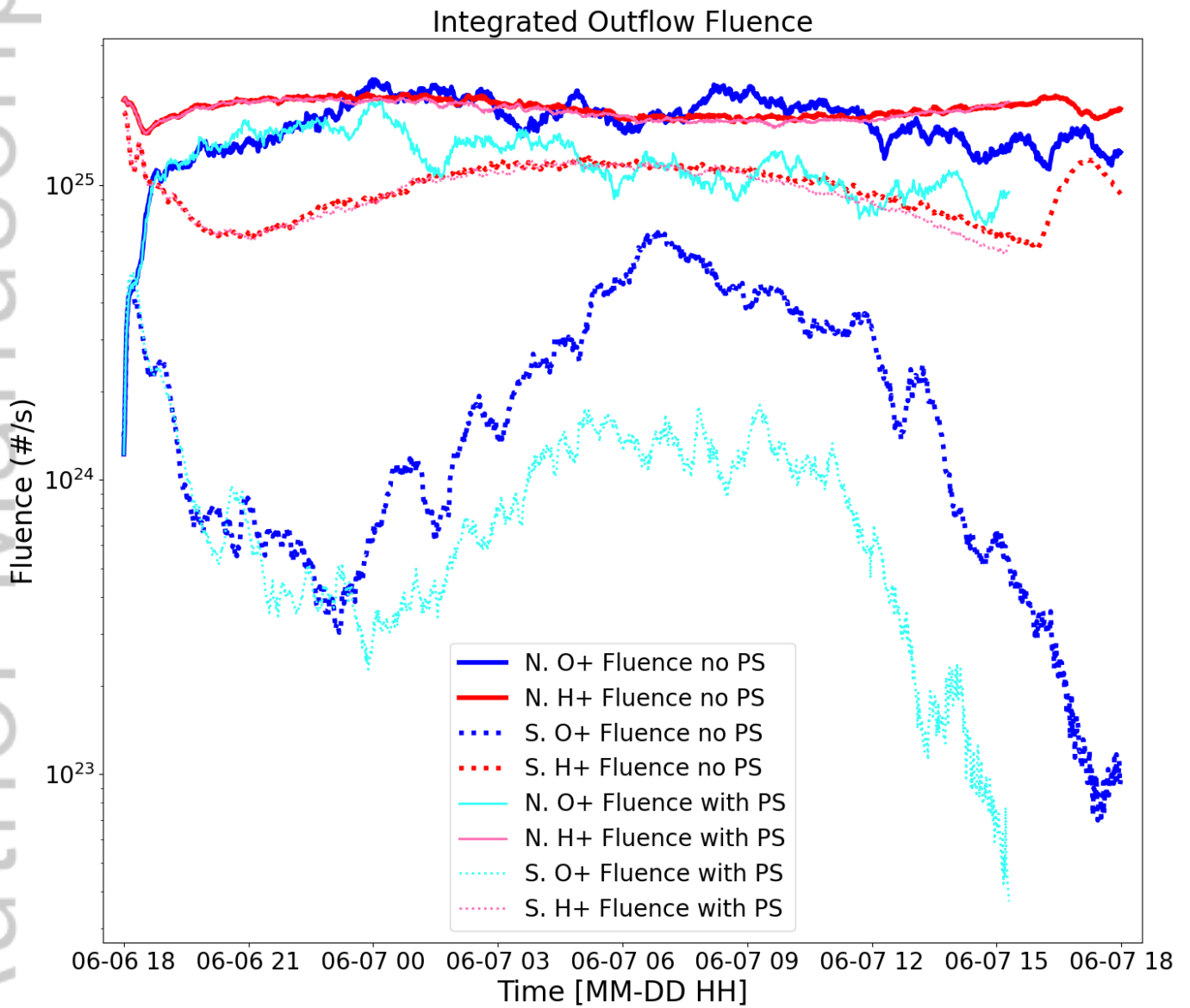
N. Precipitating Energy Flux

**e⁻
Energy
Flux:**



S. Precipitating Energy Flux

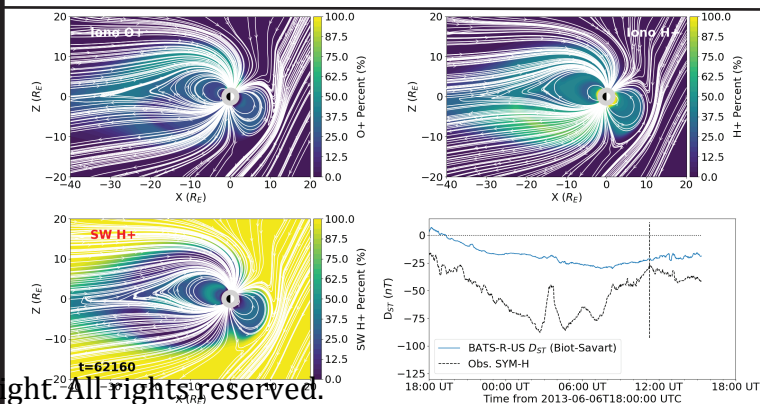
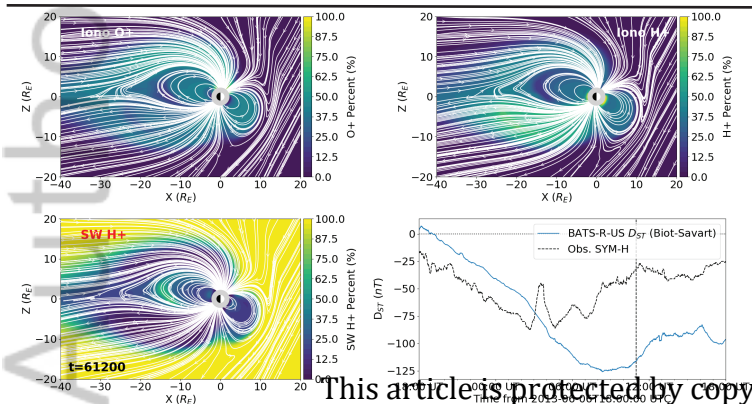
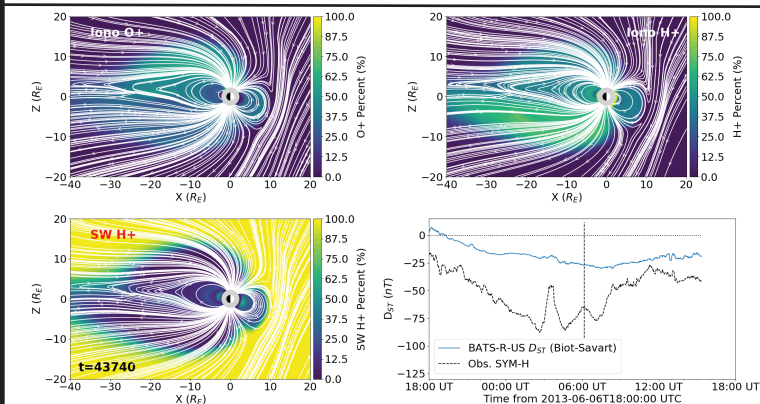
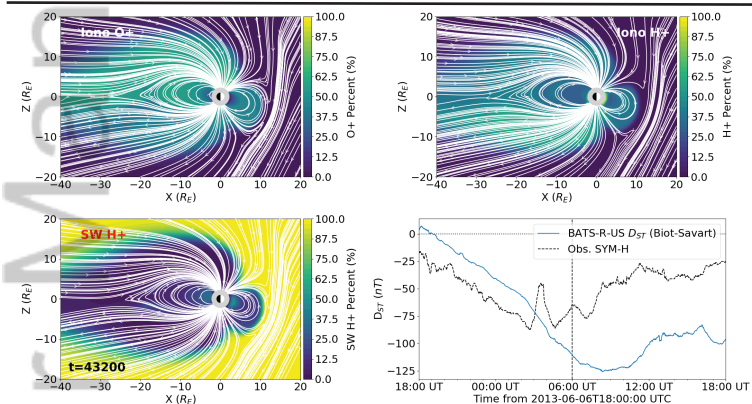
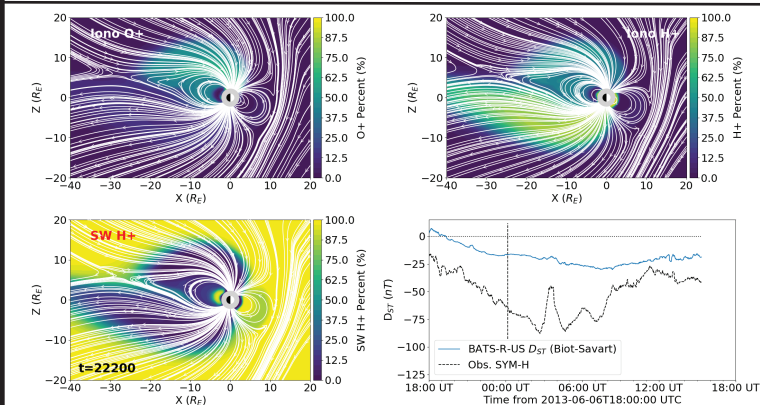
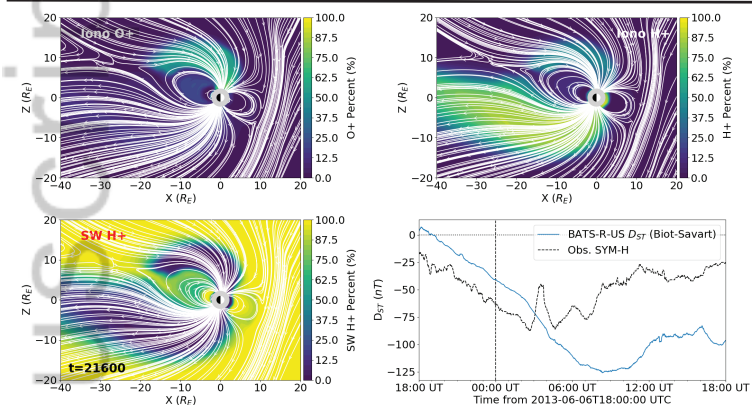




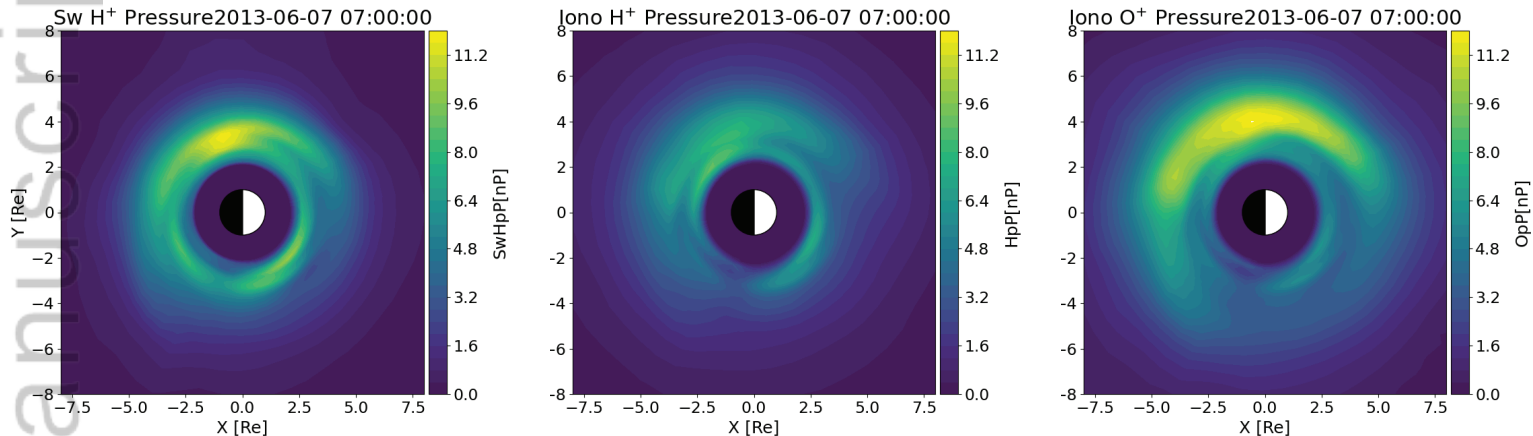
JGRA_56048_2020JA028205-f03-z-.png

Without Plasmasphere

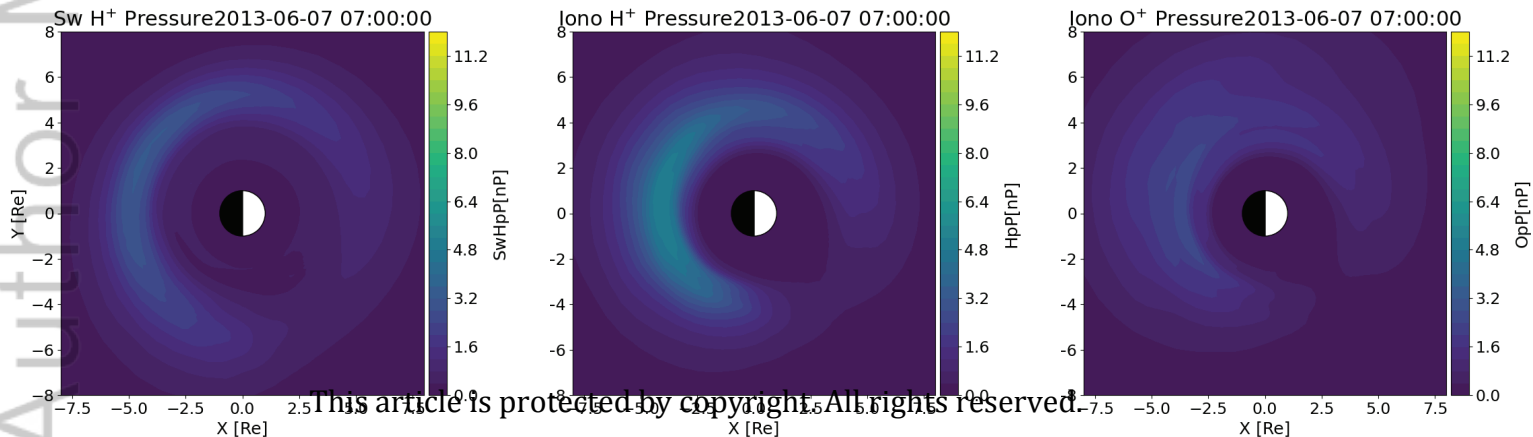
With Plasmasphere



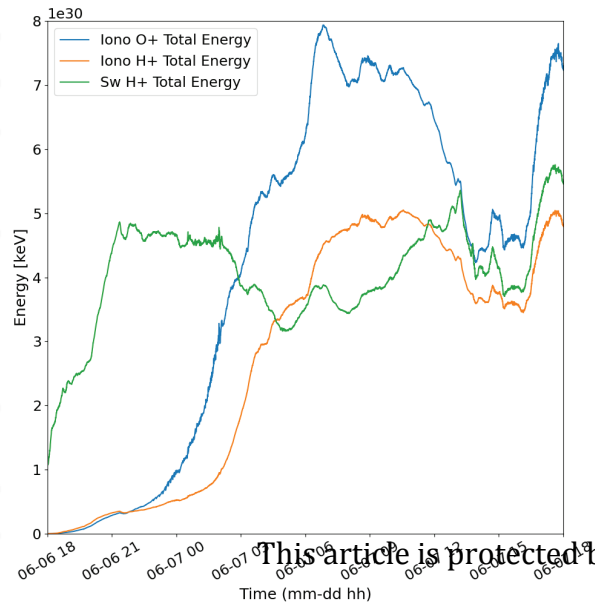
Ring Current Pressure Without Plasmasphere



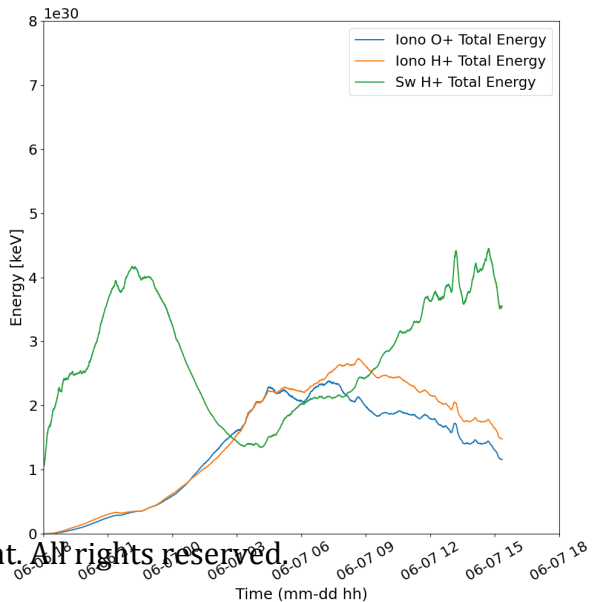
Ring Current Pressure With Plasmasphere

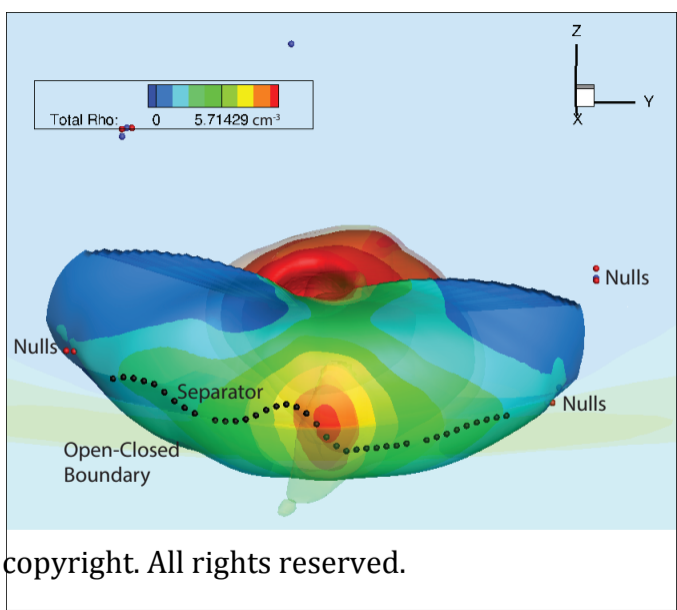
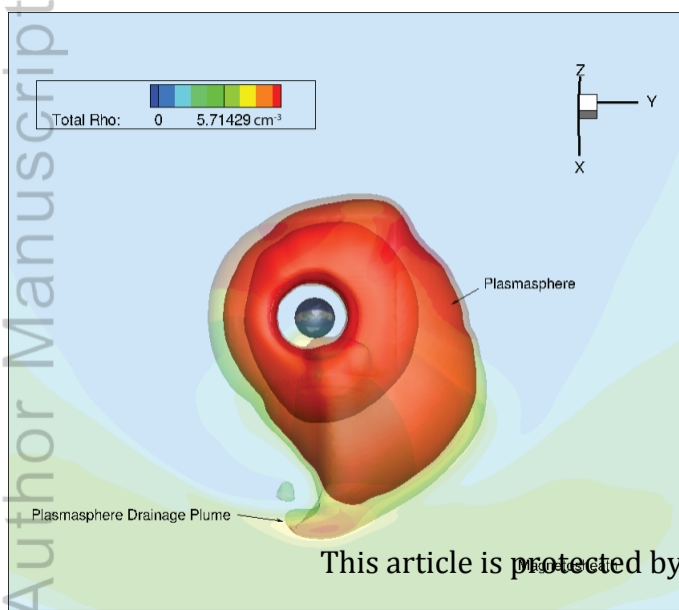


Without Plasmasphere

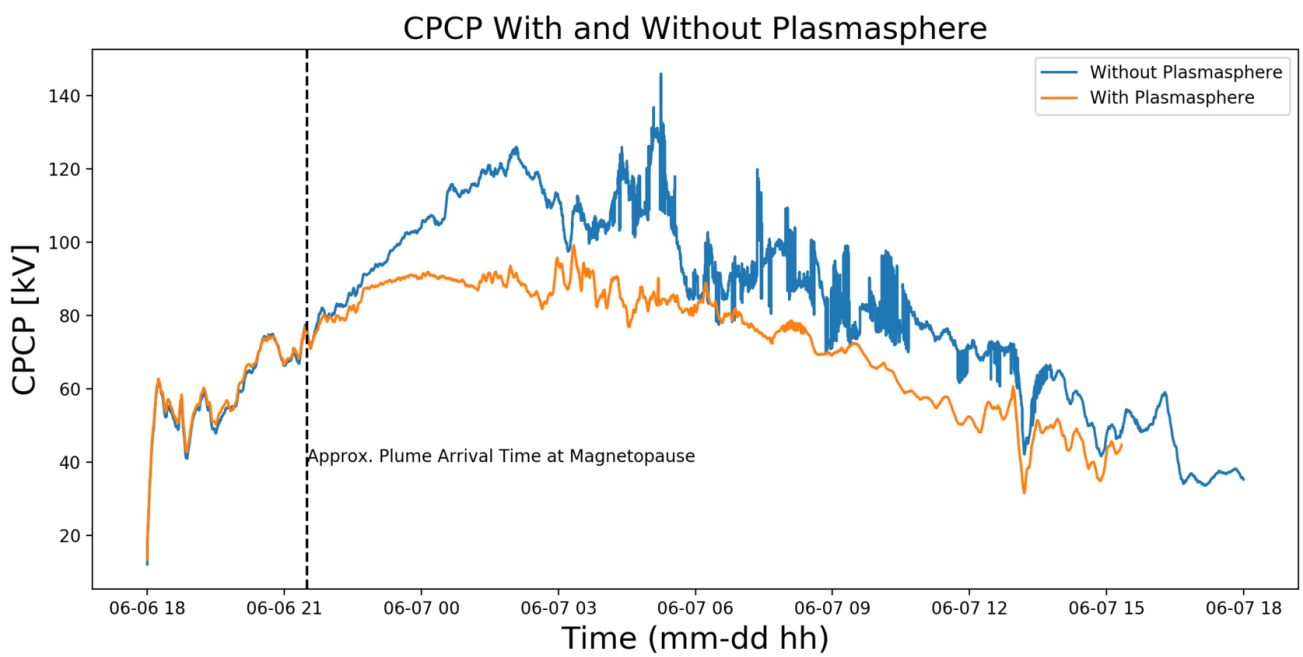


With Plasmasphere



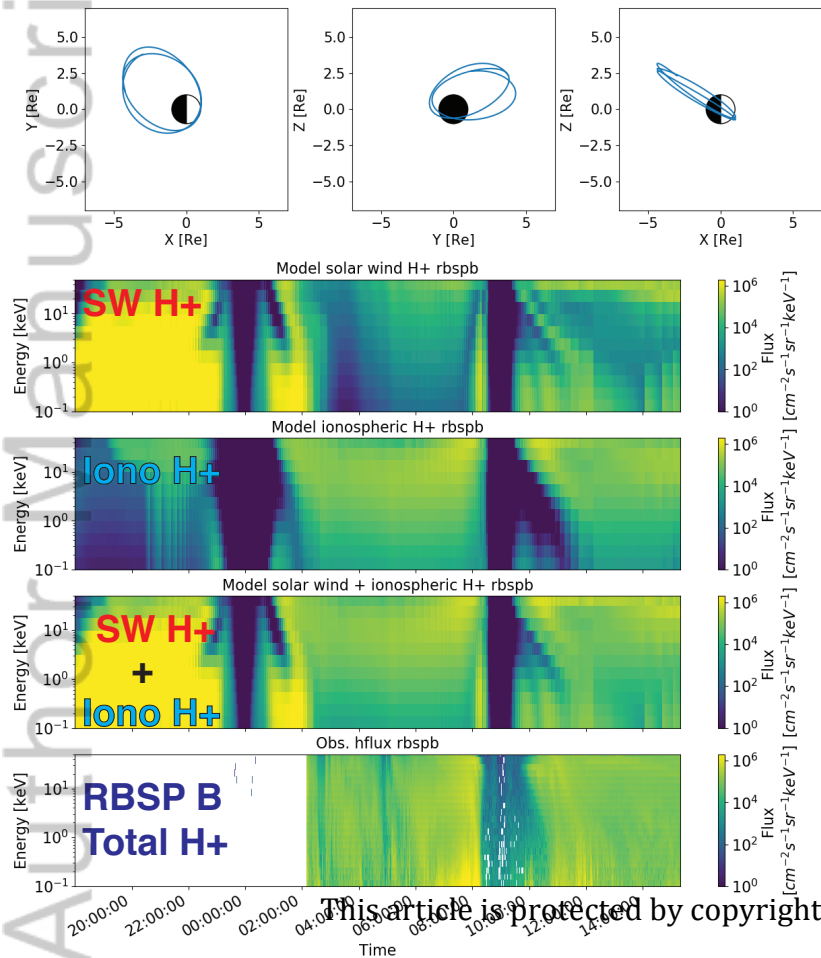


This article is protected by copyright. All rights reserved.

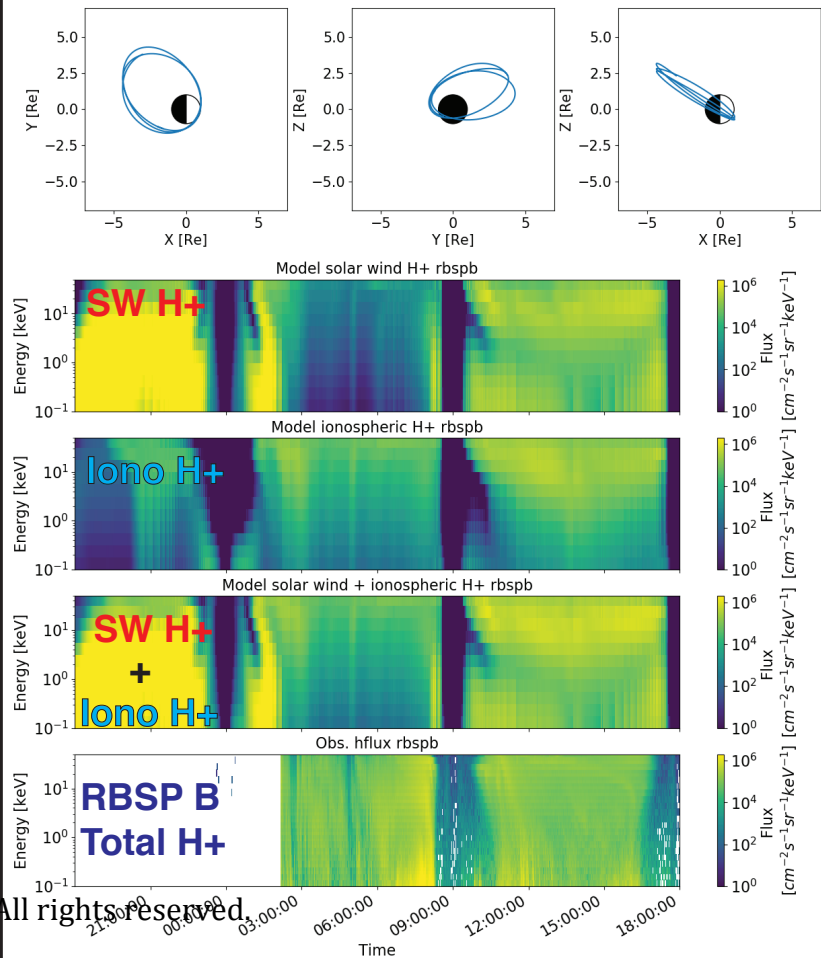


JGRA_56048_2020JA028205-f08-z-.png

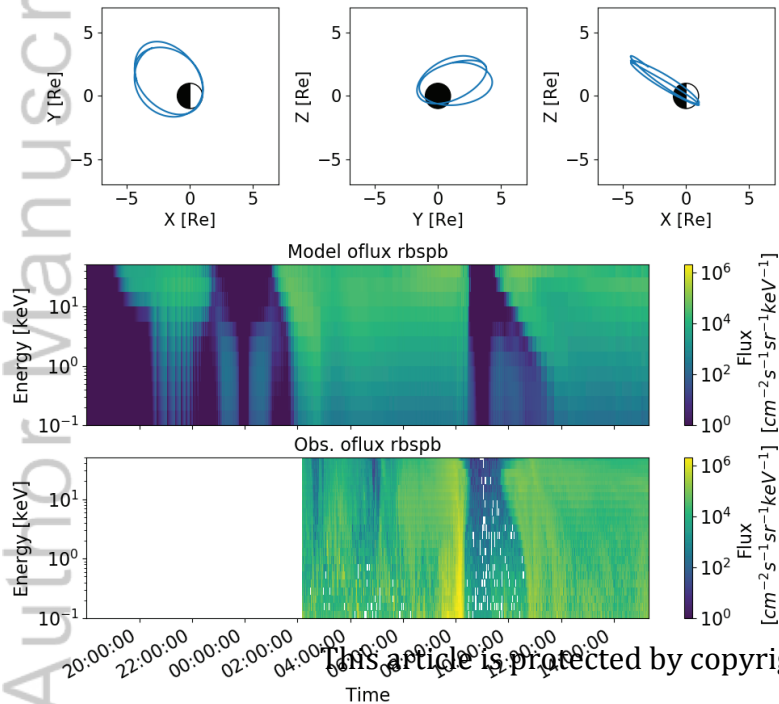
With Plasmasphere



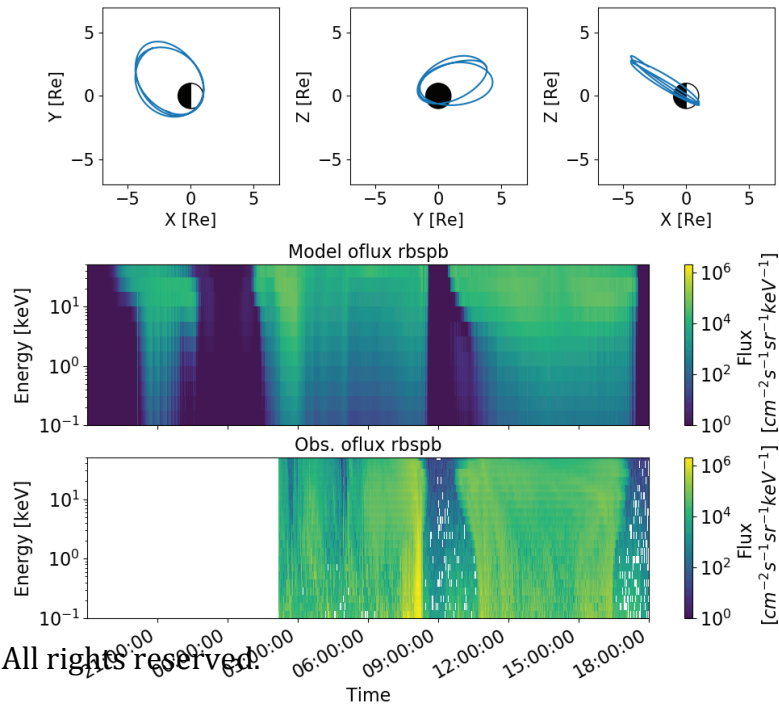
Without Plasmasphere

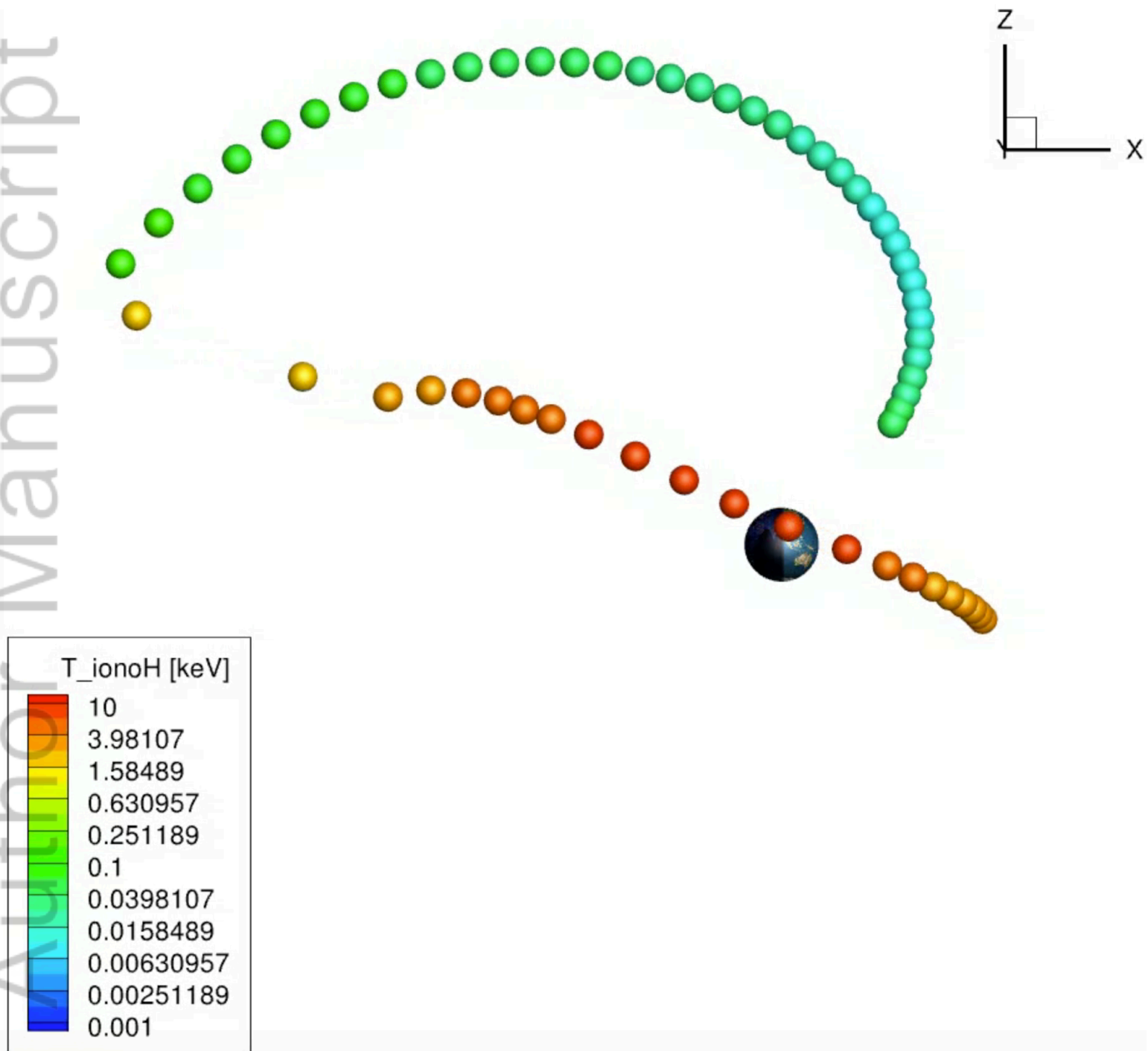


With Plasmasphere



Without Plasmasphere





JGRA_56048_2020JA028205-f11-z-.png